The Astrophysical Journal Supplement Series, 203:9 (27pp), 2012 November doi:10.1088/0067-0049/203/1/9

SPECTRAL ENERGY DISTRIBUTIONS OF LOCAL LUMINOUS AND ULTRALUMINOUS INFRARED GALAXIES

Vivian U[1,2,14,15], D. B. Sanders[1], J. M. Mazzarella[3], A. S. Evans[4,5], J. H. Howell[3,6], J. A. Surace[6], L. Armus[6], K. Iwasawa[7], D.-C. Kim[4,5], C. M. Casey[1], T. Vavilkin[8], M. Dufault[9], K. L. Larson[1], J. E. Barnes[1], B. H. P. Chan[3], D. T. Frayer[10], S. Haan[11], H. Inami[12], C. M. Ishida[1], J. S. Kartaltepe[12], J. L. Melbourne[13], and A. O. Petric[6]
[1] Institute for Astronomy, University of Hawaii, 2680 Woodlawn Drive, Honolulu, HI 96822, USA; vivian@ifa.hawaii.edu
[2] Harvard-Smithsonian Center for Astrophysics, Cambridge, MA 02138, USA
[3] Infrared Processing and Analysis Center, California Institute of Technology, 1200 E. California Blvd., Pasadena, CA 91125, USA
[4] Department of Astronomy, University of Virginia, 530 McCormick Road, Charlottesville, VA 22904, USA
[5] National Radio Astronomy Observatory, 520 Edgemont Road, Charlottesville, VA 22903, USA
[6] Spitzer Science Center, 1200 E. California Blvd., MS 314-6, California Institute of Technology, Pasadena, CA 91125, USA
[7] ICREA and Institut del Ciències del Cosmos, Universitat de Barcelona (IEEC-UB), Martí i Franquès, 1, E-08028 Barcelona, Spain
[8] Department of Physics and Astronomy, Stony Brook University, Stony Brook, NY 11794, USA
[9] Department of Astronomy, Yale University, P.O. Box 208101, New Haven, CT 06511, USA
[10] National Radio Astronomy Observatory, P.O. Box 2, Green Bank, WV 24944, USA
[11] CSIRO Astronomy and Space Science, Marsfield NSW, 2122, Australia
[12] National Optical Astronomy Observatory, 950 N. Cherry Ave., Tucson, AZ 85719, USA
[13] Caltech Optical Observatories, Division of Physics, Mathematics and Astronomy, MS 320-47, California Institute of Technology, Pasadena, CA 91125, USA
Received 2011 October 1; accepted 2012 September 2; published 2012 November 1

ABSTRACT

Luminous (LIRGs; log $(L_{\rm IR}/L_\odot) = 11.00$–$11.99$) and ultraluminous infrared galaxies (ULIRGs; log $(L_{\rm IR}/L_\odot) = 12.00$–$12.99$) are the most extreme star-forming galaxies in the universe. The local (U)LIRGs provide a unique opportunity to study their multi-wavelength properties in detail for comparison with their more numerous counterparts at high redshifts. We present common large aperture photometry at radio through X-ray wavelengths and spectral energy distributions (SEDs) for a sample of 53 nearby ($z < 0.083$) LIRGs and 11 ULIRGs spanning log $(L_{\rm IR}/L_\odot) = 11.14$–$12.57$ from the flux-limited ($f_{60\,\mu{\rm m}} > 5.24$ Jy) Great Observatories All-sky LIRG Survey. The SEDs for all objects are similar in that they show a broad, thermal stellar peak (∼0.3–2 μm), and a dominant FIR (∼40–200 μm) thermal dust peak, where $\nu L_\nu(60\,\mu{\rm m})/\nu L_\nu(V)$ increases from ∼2 to 30 with increasing $L_{\rm IR}$. When normalized at *IRAS* 60 μm, the largest range in the luminosity ratio, $R(\lambda) \equiv \log[\nu L_\nu(\lambda)/\nu L_\nu(60\,\mu{\rm m})]$, observed over the full sample is seen in the hard X-rays (HX = 2–10 keV), where $\Delta R_{\rm HX} = 3.73$ ($\bar{R}_{\rm HX} = -3.10$). A small range is found in the radio (1.4 GHz), $\Delta R_{1.4\,{\rm GHz}} = 1.75$, where the mean ratio is largest, ($\bar{R}_{1.4\,{\rm GHz}} = -5.81$). Total infrared luminosities, $L_{\rm IR}$(8–1000 μm), dust temperatures, and dust masses were computed from fitting thermal dust emission modified blackbodies to the mid-infrared (MIR) through submillimeter SEDs. The new results reflect an overall ∼0.02 dex lower luminosity than the original *IRAS* values. Total stellar masses were computed by fitting stellar population synthesis models to the observed near-infrared (NIR) through ultraviolet (UV) SEDs. Mean stellar masses are found to be $\log(M_\star/M_\odot) = 10.79 \pm 0.40$. Star formation rates have been determined from the infrared ($\rm SFR_{IR} \sim 45\,M_\odot\,yr^{-1}$) and from the monochromatic UV luminosities ($\rm SFR_{UV} \sim 1.3\,M_\odot\,yr^{-1}$), respectively. Multi-wavelength active galactic nucleus (AGN) indicators have be used to select putative AGNs: About 60% of the ULIRGs would have been classified as an AGN by at least one of the selection criteria.

Key words: galaxies: active – galaxies: interactions – galaxies: photometry – infrared: galaxies

1. INTRODUCTION

Luminous infrared galaxies (LIRGs; $L_{\rm IR}$[8–1000 μm] $\geqslant 10^{11}\,L_\odot$) are an important class of extragalactic objects. Although relatively rare in the local universe, they still outnumber optically selected starburst and Seyfert galaxies at comparable bolometric luminosity (Soifer et al. 1987), and at the highest luminosities, ultraluminous infrared galaxies, (ULIRGs; $L_{\rm IR}$[8–1000 μm] $\geqslant 10^{12}\,L_\odot$), exceed the space density of optically selected quasars by a factor of ∼3 (Sanders et al. 1988). Extensive follow-up observations at radio through X-ray wavelengths of complete samples of objects first discovered in the *IRAS* All-Sky survey, show that (U)LIRGs appear to be powered by a mixture of starburst and active galactic nucleus (AGN) activity, triggered by strong interactions and mergers of gas-rich spirals (see Sanders & Mirabel 1996, for a more complete review).

Despite the nearly two decades since the publication of the first *IRAS* catalogs of (U)LIRGs, there is surprisingly little published photometry that can be used to construct accurate spectral energy distributions (SEDs) for even the nearest and best-studied sources. The majority of the nearby (U)LIRGs are often "messy" systems that do not lend themselves to simple single aperture measurements. Published data not only suffer from different apertures used at both the same and different wavelengths, but also from inconsistent definitions of the true extent and shape of the interacting galaxies, which are often characterized by highly irregular tidal debris fields. The Great Observatories All-sky LIRG Survey (GOALS; Armus et al. 2009) has made one of its top priorities the compilation of a consistent set of photometric images of all LIRGs in the *IRAS* Revised Bright Galaxy Sample (RBGS; Sanders et al. 2003) by

[14] NASA Jenkins Predoctoral Fellow.
[15] SAO Predoctoral Fellow.

reanalyzing existing archival data and obtaining new images at radio through X-ray wavelengths.[16]

This paper presents photometric radio through X-ray SEDs for 64 of the nearest and best-studied (U)LIRGs, using common aperture "masks" to compute accurate total fluxes (including the extended tidal debris fields) for each source. These SEDs are then used to compute basic properties for each source—the total infrared (IR) luminosity, dust temperature, dust mass, and total stellar mass. We also compare SEDs of individual sources in order to understand the expected variation in spectral shapes and colors as well as AGN diagnostics for the complete sample of (U)LIRGs. Understanding the range of spectral and physical properties for this class of objects is critical before any direct comparison to their high-z counterparts can be made.

The paper is organized as follows. Descriptions of the (U)LIRG sample and of the multi-wavelength data sets are provided in Sections 2 and 3, respectively. The complete SEDs and spectral properties are presented in Section 4. Derived and adopted properties, such as the infrared luminosity, $L_{\rm IR}(8\text{–}1000\,\mu{\rm m})$, dust temperature, dust mass, and stellar mass, $M_\star$, are given in Section 5. Our conclusions are summarized in Section 6. Throughout this paper, we adopt a flat model of the universe with a Hubble constant $H_0 = 70$ km s^{-1} Mpc^{-1}, and $\Omega_{\rm m} = 0.28$, and $\Omega_\Lambda = 0.72$ (Komatsu et al. 2009).

2. SAMPLE

Our sample of 64 (U)LIRGs represents the nearest and brightest infrared-luminous extragalactic sources observable from the northern hemisphere. It is a complete subset of all objects in the *IRAS* Bright Galaxy Sample (Soifer et al. 1987), with $L_{\rm IR} > 10^{11.14}\,L_\odot$, originally chosen to satisfy the constraints $|b| > 30^\circ$ and $\delta > -30^\circ$ in order to minimize Galactic extinction and to be observable from Mauna Kea, respectively.[17] Our subsample represents 30% of all LIRGs and 50% of all ULIRGs in GOALS. The median infrared luminosity of our subsample is $\log(L_{\rm IR}/L_\odot) = 11.60$, with a luminosity range $\log(L_{\rm IR}/L_\odot) = 11.14$–$12.57$. The redshift range is $z = 0.012$–0.083, corresponding to a luminosity distance, $D_L = 50.7$–387 Mpc, with median $z = 0.028$ ($D_L = 119.0$ Mpc). Basic properties of our subsample of GOALS objects are listed in Table 1.

3. DATA

The multi-wavelength images for our targets have been assembled from a variety of sources, including our own extensive archive of ground- and space-based observations of (U)LIRGs, as well as data obtained from various data archives. The sources for the images used in our analysis is detailed in Tables 2 and 3. All images were reprocessed and analyzed using a consistent set of criteria. The procedures used to prepare the photometry masks are described in Section 3.3.

3.1. Space-based Observations

Observations of the majority of our targets at X-ray, ultraviolet, and infrared wavelengths were obtained as part of major GOALS observing campaigns. The *Chandra*-GOALS program (Iwasawa et al. 2011) provides X-ray photometry in the soft X-ray (SX; 0.5–2 KeV) and hard X-ray (HX; 2–10 KeV) bands. The *GALEX*-GOALS program (Howell et al. 2010) provides observations of the majority of our targets in the far-UV (FUV; $\lambda_{\rm eff} = 0.1528\,\mu$m) and near-UV (NUV; $\lambda_{\rm eff} = 0.2271\,\mu$m) bands. The *Spitzer*-GOALS programs (J. M. Mazzarella et al. 2012, in preparation; J. A. Surace et al. 2012, in preparation) obtained MIR (3.6, 4.6, 5.4, and 8.0 μm) and FIR (24, 70, and 160 μm) images with IRAC and MIPS, respectively. The *Herschel*-GOALS programs (PIs: Sanders and Armus) involving PACS and SPIRE observations are currently ongoing and will be completed in late 2012. *IRAS* data at 12, 25, 60, and 100 μm as published in the RBGS (Sanders et al. 2003) have also been incorporated into our analysis for completeness.

3.2. Ground-based Observations

Most of the observations in the optical bands were taken with the Tektronix 2048 × 2048 camera (hereafter, Tek2048) at the University of Hawaii (UH) 2.2 m Telescope on Mauna Kea. *BVI*-band images for 53 LIRGs + 1 ULIRG were originally obtained as part of a PhD thesis that studied a complete subsample of LIRGs from the *IRAS* BGS (see Ishida 2004, for details on the observations and reduction). The primary source of the *R*-band images is the RBGS *R*-*K*′ Atlas (J. M. Mazzarella et al. 2012, in preparation), while Surace et al. (1998, 2000) and Surace & Sanders (2000) provide *UBI*-band data for many of the ULIRGs, all imaged with either the Tek2048 or the Orbit 2048 × 2048 cameras on the UH 2.2 m Telescope.

The remaining optical, near-infrared (NIR), submillimeter, and radio data have been compiled from the literature and the NASA/IPAC Extragalactic Database (NED). Most notably, JHK_S images were extracted from the Two Micron All Sky Survey (2MASS; Skrutskie et al. 2006) Extended Source Image Server, and in the case of large systems spanning multiple frames, the Large Galaxy Atlas (Jarrett et al. 2003) via the InfraRed Science Archive. Submillimeter data at 850 μm and 450 μm, obtained using the Submillimeter Common-User Bolometer Array (SCUBA) at the James Clerk Maxwell Telescope were taken from Dunne et al. (2000) and Dunne & Eales (2001), while 1.49 GHz radio data obtained at the Very Large Array (VLA) were taken from Condon et al. (1990, 1996). All of our archival data sources are summarized in Table 2.

The remaining gaps in our optical photometry table were filled by observed with the Tek2048 camera on the UH 2.2 m Telescope during two observing runs, totaling eight partially photometric nights in February and August of 2008. Each exposure was typically 2–6 minutes, with seeing ranging between 0.″5 and 0.″8, (see Table 3 for a summary). A dither pattern of 80.″0 × 80.″0 was used during the observations. The data were reduced and calibrated using various packages provided by the IDL astron library. The reduction involved several standard steps: All images were bias subtracted using a median bias computed from bias frames taken at the beginning of each night. There is a location-dependent shutter correction time of 0.18 s (H. Courtois 2008, private communication) for the Tek2048; this is a significant contribution for the images with short exposure times (calibration stars in particular), so all of the data were corrected by this factor. For each of the *UVRI* filters during each night of the run, a master flat, created from median-combining normalized flats, was used to flat field all the corresponding science images. After adding astrometry information (using IDL routine STARAST) to the image headers, science images observed close in time within

[16] A complete description of the multi-wavelength data can be found on the GOALS Web site at http://www.goals.ipac.caltech.edu.

[17] NGC 1068 would have been a part of this sample. However, its proximity, and thus large angular extent, pose a challenge for the UH 2.2 m Telescope and its limited field of view to capture the entire galaxy and its full debris field. Therefore, it has been left out of the current sample.

Table 1
Local (U)LIRG Sample

RBGS Name	R.A. (J2000)	Decl. (J2000)	$\log(L_{\rm IR})_{IRAS}$ ($L_\odot$)	D_L (Mpc)	Other Names
NGC 0034	00 11 06.5	−12 06 26	11.49	84.1	NGC 0017, VV 860, Mrk 0938
MCG -02-01-051/2	00 18 50.4	−10 22 08	11.48	117.5	Arp 256, VV 352
NGC 0232	00 42 45.8	−23 33 41	11.44	95.2	VV 830
IC 1623A/B	01 07 47.2	−17 30 25	11.71	85.5	Arp 236, VV 114
MCG -03-04-014	01 10 08.9	−16 51 10	11.65	144.0	
CGCG 436-030	01 20 02.7	+14 21 43	11.69	134.0	
IRAS F01364-1042	01 38 52.9	−10 27 11	11.85	210.0	
III Zw 035	01 44 30.5	+17 06 05	11.64	119.0	
NGC 0695	01 51 14.2	+22 34 57	11.68	139.0	UGC 01315, V Zw 123
NGC 0958	02 30 42.8	−02 56 20	11.20	80.6	
UGC 02238	02 46 17.5	+13 05 44	11.33	92.4	
UGC 02369	02 54 01.8	+14 58 25	11.67	136.0	
IRAS F03359+1523	03 38 46.7	+15 32 55	11.55	152.0	
UGC 02982	04 12 22.4	+05 32 51	11.20	74.9	
ESO 550-IG025	04 21 20.0	−18 48 48	11.51	138.5	
NGC 1614	04 33 59.8	−08 34 44	11.65	67.8	Arp 186, Mrk 0617, II Zw 015
IRAS F05189-2524	05 21 01.5	−25 21 45	12.16	187.0	
NGC 2623	08 38 24.1	+25 45 17	11.60	84.1	UGC 04509, Arp 243, VV 079
IRAS F08572+3915	09 00 25.4	+39 03 54	12.16	264.0	
UGC 04881	09 15 55.1	+44 19 55	11.74	178.0	Arp 055, VV 155
UGC 05101	09 35 51.6	+61 21 11	12.01	177.0	
MCG +08-18-012/3	09 36 37.2	+48 28 28	11.34	117.0	CGCG 239-011
IC 0563/4	09 46 20.6	+03 03 30	11.23	92.9	UGC 05230, Arp 303
NGC 3110	10 04 02.1	−06 28 29	11.37	79.5	NGC 3122, NGC 3518
IRAS F10173+0828	10 20 00.2	+08 13 34	11.86	224.0	
IRAS F10565+2448	10 59 18.1	+24 32 35	12.08	197.0	
MCG +07-23-019	11 03 53.2	+40 50 57	11.62	158.0	Arp 148, VV 032
CGCG 011-076	11 21 12.2	−02 59 03	11.43	117.0	
IC 2810A/B	11 25 45.0	+14 40 36	11.64	157.0	UGC 06436
NGC 3690/IC 694	11 28 30.4	+58 34 10	11.93	50.7	Arp 299, VV 118
IRAS F12112+0305	12 13 46.0	+02 48 38	12.36	340.0	
IRAS F12224-0624	12 25 03.9	−06 40 53	11.36	125.0	
UGC 08058	12 56 14.2	+56 52 25	12.57	192.0	Mrk 0231, VII Zw 490
NGC 4922	13 01 24.9	+29 18 40	11.38	111.0	UGC 08135, VV 609
ESO 507-G070	13 02 52.3	−23 55 18	11.56	106.0	
IC 0860	13 15 03.5	+24 37 08	11.14	56.8	
VV 250	13 15 32.8	+62 07 37	11.81	142.0	UGC 08335, Arp 238, VII Zw 506
UGC 08387	13 20 35.3	+34 08 22	11.73	110.0	IC 0883, Arp 193, VV 821, I Zw 056
NGC 5104	13 21 23.1	+00 20 33	11.27	90.8	UGC 08391
MCG -03-34-064	13 22 24.4	−16 43 43	11.28	82.2	
NGC 5135	13 25 44.0	−29 50 01	11.30	60.9	
NGC 5256	13 38 17.5	+48 16 37	11.56	129.0	UGC 08632, Mrk 0266, I Zw 067
NGC 5257/8	13 39 55.2	+00 50 13	11.62	108.5	Arp 240, VV 055
UGC 08696	13 44 42.1	+55 53 13	12.21	173.0	Mrk 0273, VV 851, I Zw 071
CGCG 247-020	14 19 43.2	+49 14 12	11.39	120.0	Mrk 1490
IRAS F14348-1447	14 37 38.3	−15 00 23	12.39	387.0	
VV 340	14 57 00.4	+24 36 44	11.74	157.0	UGC 09618, Arp 302
CGCG 049-057	15 13 13.1	+07 13 32	11.35	65.4	
VV 705	15 18 06.3	+42 44 37	11.92	183.0	Mrk 0848, I Zw 107
IRAS F15250+3608	15 26 59.4	+35 58 38	12.08	254.0	
UGC 09913	15 34 57.1	+23 30 11	12.28	87.9	Arp 220, VV 540
NGC 6090	16 11 40.7	+52 27 24	11.58	137.0	UGC 10267, VV 626, Mrk 0496, I Zw 135
CGCG 052-037	16 30 56.5	+04 04 58	11.45	116.0	
NGC 6285/6	16 58 27.8	+58 56 48	11.37	85.7	Arp 293
IRAS F17132+5313	17 14 20.0	+53 10 30	11.96	232.0	
ESO 602-G025	22 31 25.5	−19 02 04	11.34	110.0	
IRAS F22491-1808	22 51 49.2	−17 52 23	12.20	351.0	
NGC 7469/IC 5283	23 03 16.9	+08 53 01	11.65	70.8	Arp 298, UGC 12332
CGCG 453-062	23 04 56.5	+19 33 08	11.38	109.0	
IC 5298	23 16 00.7	+25 33 24	11.60	119.0	
NGC 7592	23 18 22.2	+04 25 01	11.40	106.0	VV 731
NGC 7674	23 27 57.8	+08 46 51	11.56	125.0	UGC 12608, Arp 182, VV 343, Mrk 0533
NGC 7770/1	23 51 24.9	+20 06 43	11.40	61.2	UGC 12815, Mrk 9006
MRK 0331	23 51 26.8	+20 35 10	11.50	70.5	

Note. The $L_{\rm IR}$ column indicates infrared luminosities based on *IRAS* measurements only.

Table 2
Major Data Sets

Telescope	No. of Objects	Bands	Reference
Chandra	22	0.5–2 keV, 2–10 keV	Iwasawa et al. (2011)
GALEX	57	NUV, FUV	Howell et al. (2010)
UH 2.2m	64	B, V, I	Ishida (2004)
UH 2.2m	8	U, B	Surace et al. (1998, 2000); Surace & Sanders (2000)
UH 2.2m	46	R	J. M. Mazzarella et al. (2012, in preparation)
2MASS	64	J, H, K_s	Skrutskie et al. (2006); Jarrett et al. (2003)
Spitzer	64	3.6, 4.5, 5.8, 8.0, 24, 70, 160 μm	J. M. Mazzarella et al. (2012, in preparation); J. A. Surace et al. (2012, in preparation)
IRAS	64	12, 25, 60, 100 μm	Sanders et al. (2003)
JCMT/SCUBA	42	450, 850 μm	Dunne et al. (2000); Dunne & Eales (2001)
VLA	64	1.49, 4.85 GHz	Condon et al. (1990, 1996)

Table 3
New UH 2.2 m Observations

RBGS Name	Exp. Time (s)	Filter (Johnson)	Seeing (arcsec)	Obs. Date (UT)
CGCG 436-030	180	R	0.″7	2008 Sep 1
IRAS F01364-1042	360	U	0.″6	2008 Aug 28
NGC 0695	180	R	0.″7	2008 Sep 1
IRAS F05189-2524	180	V	0.″6	2008 Sep 1
	180	I	0.″6	2008 Sep 1
IRAS F08572+3915	180	V	0.″7	2008 Feb 15
IRAS F10565+2448	330	U	0.″6	2008 Feb 18 and 19
	180	V	0.″7	2008 Feb 18
IRAS F12112+0305	180	V	0.″5	2008 Feb 19
UGC 08058	120	I	0.″8	2008 Feb 16
UGC 08696	120	V	0.″5	2008 Feb 17
IRAS F14348-1447	180	V	0.″7	2008 Feb 15
IRAS F22491-1808	180	V	0.″7	2008 Aug 28

the same night were co-added to increase the signal-to-noise ratio for each target frame. The data were subsequently calibrated with standard stars in the corresponding optical bands (Landolt 1983), taking into account airmass corrections. To ensure that consistent apertures were used to find the total flux from each galaxy system, photometry was subsequently measured using previously constructed "masks," as described in Section 3.3.

3.3. Photometry Masks

When assembling SEDs for our sources, we constructed a single photometric mask for each source that was designed to incorporate the total flux from a galaxy system whether it consists of a single galaxy with disturbed morphology or two separate interacting galaxies. The masks have been defined based on isophotes in the median- and boxcar-smoothed I-band images at the surface brightness limit of 24.5 mag arcsec^{-2} (Vavilkin et al. 2011). They are intended to encapsulate the global flux from tidal debris as well as individual components within these merger systems. The more luminous 43 objects in our sample ($L_{IR} > 11.4$) have masks defined using *HST*-ACS images (A. S. Evans et al. 2012, in preparation); the other 21 masks were generated using the same technique from ground-based I-band images taken with the UH 2.2 m Telescope. We have tested for systematic bias between the masks made from *Hubble Space Telescope* (*HST*) and ground-based images and found that the difference in measured photometry is less than 0.2%, within photometric uncertainties. The photometry masks for all 64 (U)LIRGs are shown in Figure 1.

Masked photometry has been extracted from images taken at effective wavelength $0.15\,\mu\text{m} < \lambda_{\text{eff}} < 8\,\mu\text{m}$ and at MIPS 24 μm band. The short wavelength limit has been imposed due to the fact that the X-ray photon counts are fairly localized, whereas on the longward side, the images are lacking in resolution ($\gtrsim$6.″0 point spread function). At either end of the wavelength range, therefore, masks would not improve the precision of the total flux measurement over that of circular or elliptical apertures. Differential emission will be taken into account when deep optical/NIR images probing the extended debris field are acquired in the near future (*Spitzer* snapshot program; PI: Sanders). Within the wavelength regime where masks have been applied, the masks are very large relative to the beam size and hence aperture corrections are not needed.

4. SPECTRAL ENERGY DISTRIBUTION OF THE GOALS SAMPLE

In this section, we present SEDs (radio through X-ray) for our complete sample of 64 (U)LIRGs. The common aperture mask photometry data are provided in Table 4 (X-ray to NIR) and Table 5 (MIR to radio). The complete radio through X-ray SEDs ($\log \nu L_\nu$ versus $\log \nu$) for each source are shown in the panels of Figure 2. The photometric data points are overlaid with the best-fit model SEDs, which will be discussed in more detail in Section 5.1.

(U)LIRGs are known to exhibit several common features in their SEDs, e.g., a drop-off in the UV flux, an optical-NIR stellar thermal "bump," and a thermal dust "bump" at FIR wavelengths (Sanders & Mirabel 1996). However, photometry compiled for our complete local sample displays varied spectral shapes across the electromagnetic spectrum. The main goal of our current study is to characterize the full SED and spectral properties of (U)LIRGs as follows.

4.1. Spectral Shapes

Before we employ the SEDs of these (U)LIRGs as local templates, we must first understand the variations in the spectral shapes across the range of various attributes. In particular, Figure 3 shows the radio through X-ray SEDs of all 64 (U)LIRGs. Normalized at J band, this plot shows the best-fit modeled fluxes at the observed filters and brings out the variations in the optical (UV–NIR) regime, the shortward end of which at FUV is characterized by the young stellar populations in the galaxies. No attempt has been made to connect the observed X-ray emission to the UV flux given our lack of data in the nearly two decade wavelength range between the FUV and SX measurements.

To better demonstrate both the range and mean of the object SEDs, we show in Figure 4 the mean SED along with the 25%, 75%, and max/min values for the 11 ULIRGs and 53 LIRGs

Table 4
Local (U)LIRG Photometry (Jy; $\lambda < 3\ \mu$m)

RBGS Name	HX 2–10 KeV	SX 0.5–2 KeV	FUV 152.8 Å	NUV 227.1 Å	*U* 3655 Å	*B* 4582 Å	*V* 5377 Å	*R* 6484 Å	*I* 8570 Å	*J* 1.241 μm	*H* 1.651 μm	K_s 2.165 μm
(1)	(2)	(3)	(4)	(5)	(6)	(7)	(8)	(9)	(10)	(11)	(12)	(13)
NGC 0034	1.586E-08[a]	2.318E-08[a]	5.249E-04	1.262E-03	...	1.076E-02	1.629E-02	1.740E-02	2.679E-02	5.225E-02	6.529E-02	6.557E-02
	(...)	(...)	(6.480E-05)	(7.126E-05)	(...)	(5.949E-04)	(9.004E-04)	(1.122E-03)	(1.481E-03)	(1.357E-04)	(2.097E-04)	(1.783E-04)
MCG -02-01-051/2	...	...	2.255E-03	3.279E-03	...	1.028E-02	1.368E-02	...	2.032E-02	3.552E-02	3.808E-02	3.247E-02
	(...)	(...)	(2.784E-04)	(1.851E-04)	(...)	(1.136E-03)	(1.512E-03)	(...)	(2.246E-03)	(1.287E-04)	(3.044E-04)	(2.060E-04)
NGC 0232	...	...	2.038E-04	3.880E-04	...	1.535E-02	3.071E-02	1.461E-02	6.925E-02	6.128E-02	8.037E-02	7.487E-02
	(...)	(...)	(1.538E-05)	(1.637E-05)	(...)	(2.097E-03)	(2.220E-03)	(9.417E-04)	(1.148E-02)	(9.594E-04)	(1.480E-03)	(1.448E-03)
IC 1623A/B	...	...	5.624E-03	7.898E-03	...	1.871E-02	2.489E-02	3.569E-02	3.467E-02	6.292E-02	7.755E-02	7.716E-02
	(...)	(...)	(6.942E-04)	(4.459E-04)	(...)	(1.034E-03)	(1.375E-03)	(2.301E-03)	(1.916E-03)	(1.304E-04)	(1.906E-04)	(1.958E-04)
MCG -03-04-014	...	...	2.402E-04	5.692E-04	...	4.093E-03	6.792E-03	8.801E-03	1.169E-02	3.336E-02	4.045E-02	3.829E-02
	(...)	(...)	(2.965E-05)	(3.213E-05)	(...)	(2.639E-04)	(4.379E-04)	(5.674E-04)	(6.463E-04)	(1.085E-04)	(1.456E-04)	(1.494E-04)
CGCG 436-030	...	...	4.304E-04	7.831E-04	...	4.130E-03	6.310E-03	8.075E-03	1.019E-02	1.702E-02	2.365E-02	2.286E-02
	(...)	(...)	(5.313E-05)	(4.421E-05)	(...)	(3.424E-04)	(4.649E-04)	(1.487E-03)	(2.064E-03)	(9.198E-05)	(1.101E-04)	(1.610E-04)
IRAS F01364-1042	1.961E-09	1.506E-09	2.456E-05	5.314E-05	4.786E-05	5.989E-04	1.223E-03	9.056E-04	2.239E-03	6.269E-03	7.249E-03	8.223E-03
	(...)	(...)	(2.738E-06)	(2.811E-06)	(2.047E-05)	(7.347E-05)	(8.546E-05)	(5.839E-05)	(3.013E-04)	(5.634E-05)	(7.102E-05)	(7.910E-05)
III Zw 035	...	...	5.246E-05	1.132E-04	...	1.570E-03	2.911E-03	2.111E-03	5.495E-03	1.176E-02	1.484E-02	1.485E-02
	(...)	(...)	(6.476E-06)	(6.390E-06)	(...)	(1.012E-04)	(1.877E-04)	(1.361E-04)	(6.074E-04)	(5.151E-05)	(6.033E-05)	(6.564E-05)
NGC 0695	...	...	3.526E-04	7.967E-04	...	7.727E-03	1.343E-02	1.830E-02	2.655E-02	4.630E-02	5.962E-02	5.437E-02
	(...)	(...)	(4.352E-05)	(4.498E-05)	(...)	(7.828E-04)	(3.710E-04)	(3.370E-03)	(7.335E-04)	(1.001E-04)	(1.188E-04)	(1.226E-04)
NGC 0958	...	...	1.084E-03[a]	2.079E-03	1.959E-02	2.128E-02	3.837E-02	...	8.318E-02	1.798E-01	2.335E-01	2.013E-01
	(...)	(...)	(7.689E-06)	(6.549E-06)	(2.526E-03)	(1.176E-03)	(2.120E-03)	(...)	(3.830E-03)	(1.988E-03)	(3.226E-03)	(3.709E-03)
UGC 02238	...	...	1.092E-04	2.096E-04	...	3.873E-03	7.311E-03	...	1.660E-02	3.430E-02	4.897E-02	5.267E-02
	(...)	(...)	(5.382E-06)	(4.912E-06)	(...)	(1.427E-04)	(2.020E-04)	(...)	(4.586E-04)	(8.845E-04)	(1.037E-03)	(1.407E-03)
UGC 02369	...	...	...	...	...	5.058E-03	1.138E-02	1.344E-02	2.704E-02	5.274E-02	6.806E-02	6.325E-02
	(...)	(...)	(...)	(...)	(...)	(1.398E-04)	(2.096E-04)	(8.668E-04)	(1.245E-03)	(1.330E-04)	(2.199E-04)	(1.806E-04)
IRAS F03359+1523	...	...	1.054E-04	1.905E-04	...	1.019E-03	1.770E-03	...	3.404E-03	7.850E-03	1.001E-02	...
	(...)	(...)	(1.302E-05)	(1.075E-05)	(...)	(8.443E-05)	(1.630E-04)	(...)	(2.195E-04)	(4.966E-05)	(5.567E-05)	(...)
UGC 02982	...	...	3.468E-05	4.028E-05	...	1.690E-03	4.699E-03	9.651E-03	1.259E-02	5.635E-02	7.398E-02	7.920E-02
	(...)	(...)	(3.076E-05)	(1.637E-05)	(...)	(1.090E-04)	(1.731E-04)	(6.222E-04)	(4.638E-04)	(1.349E-03)	(1.976E-03)	(2.261E-03)
ESO 550-IG025	...	...	1.992E-04	4.222E-04	...	3.873E-03	7.178E-03	7.187E-03	1.445E-02	3.564E-02	4.766E-02	3.978E-02
	(...)	(...)	(2.459E-05)	(2.384E-05)	(...)	(2.140E-04)	(3.967E-04)	(4.634E-04)	(7.988E-04)	(1.120E-04)	(3.408E-04)	(1.785E-04)
NGC 1614	...	...	...	...	1.307E-02[a]	1.330E-02	2.188E-02	3.255E-02[a]	4.246E-02	9.204E-02	1.173E-01	1.127E-01
	(...)	(...)	(...)	(...)	(1.686E-04)	(9.803E-04)	(1.209E-03)	(5.996E-04)	(2.347E-03)	(1.678E-04)	(2.079E-04)	(2.372E-04)
IRAS F05189-2524	2.143E-07	2.691E-08	8.816E-05	2.079E-04	1.905E-03[b]	2.291E-03[b]	2.589E-03	5.065E-03	7.805E-03	1.698E-02	2.655E-02	4.770E-02
	(...)	(...)	(1.088E-05)	(1.174E-05)	(3.510E-04)	(4.220E-04)	(4.770E-04)	(3.265E-04)	(3.595E-03)	(8.018E-05)	(1.383E-04)	(1.273E-04)
NGC 2623	...	...	3.904E-04	7.948E-04	5.592E-03[a]	7.656E-03	1.282E-02	1.797E-02[a]	2.188E-02	3.795E-02	5.127E-02	4.667E-02
	(...)	(...)	(4.820E-05)	(4.487E-05)	(1.082E-04)	(2.115E-04)	(3.543E-04)	(3.476E-04)	(4.030E-04)	(1.127E-04)	(2.758E-04)	(1.670E-04)
IRAS F08572+3915	1.654E-09	3.177E-09	8.223E-05	1.269E-04	6.918E-04[b]	6.710E-04[b]	8.158E-04	9.651E-04	1.710E-03[a]	3.113E-03	3.342E-03	4.581E-03
	(...)	(...)	(1.015E-05)	(7.164E-06)	(1.274E-04)	(1.233E-05)	(2.254E-04)	(6.222E-05)	(1.353E-05)	(3.883E-05)	(5.757E-05)	(5.571E-05)
UGC 04881	9.824E-10	4.542E-09	2.150E-04	4.792E-04	...	4.325E-03	7.586E-03	...	1.486E-02	3.011E-02	3.465E-02	3.689E-02
	(...)	(...)	(2.654E-05)	(2.705E-05)	(...)	(2.390E-04)	(4.891E-04)	(...)	(8.212E-04)	(1.041E-04)	(1.203E-04)	(1.406E-04)
UGC 05101	8.647E-09	6.183E-09	5.977E-05	1.800E-04	1.586E-03[a]	2.874E-03[a]	5.124E-03[a]	1.434E-02	1.0547E-02[a]	2.233E-02	3.087E-02	3.960E-02
	(...)	(...)	(7.378E-06)	(1.016E-05)	(5.990E-05)	(4.9097E-05)	(1.463E-04)	(9.245E-04)	(9.7144E-05)	(9.444E-05)	(1.312E-04)	(1.357E-04)
MCG +08-18-013	...	...	7.505E-04	1.063E-03	...	5.808E-03	8.954E-03	...	1.675E-02	2.152E-03	3.133E-03	2.288E-03
	(...)	(...)	(3.076E-05)	(1.637E-05)	(...)	(5.349E-04)	(6.597E-04)	(...)	(1.388E-03)	(2.696E-04)	(4.414E-04)	(4.342E-04)
IC 0563/4	...	...	3.575E-04	6.942E-04	...	1.247E-02	2.148E-02	3.1685E-02	4.571E-02	8.131E-02	1.042E-01	9.629E-02
	(...)	(...)	(2.307E-05)	(1.637E-05)	(...)	(8.042E-04)	(1.187E-03)	(5.837E-04)	(2.526E-03)	(3.162E-04)	(4.702E-04)	(3.714E-04)

Table 4
(Continued)

RBGS Name	HX	SX	FUV	NUV	*U*	*B*	*V*	*R*	*I*	*J*	*H*	K_s
	2–10 KeV	0.5–2 KeV	152.8 Å	227.1 Å	3655 Å	4582 Å	5377 Å	6484 Å	8570 Å	1.241 μm	1.651 μm	2.165 μm
(1)	(2)	(3)	(4)	(5)	(6)	(7)	(8)	(9)	(10)	(11)	(12)	(13)
NGC 3110	...	...	1.384E-03	2.734E-03	...	1.794E-02	2.731E-02	1.517E-02[a]	5.077E-02	9.130E-02	1.142E-01	1.031E-01
	(...)	(...)	(4.613E-05)	(3.275E-05)	(...)	(3.605E-03)	(3.018E-03)	(1.397E-03)	(5.423E-03)	(1.850E-03)	(2.418E-03)	(2.943E-03)
IRAS F10173+0828	7.582E-11	6.067E-10	1.678E-06	8.517E-06	...	4.406E-04	1.009E-03	2.758E-03	2.249E-03	3.817E-03	4.703E-03	3.315E-03
	(...)	(...)	(2.072E-07)	(4.809E-07)	(...)	(2.840E-05)	(5.577E-05)	(1.778E-04)	(1.036E-04)	(4.416E-05)	(5.791E-05)	(6.045E-05)
IRAS F10565+2448	2.376E-09	8.557E-09	...	...	2.160E-03	3.862E-03[a]	5.541E-03	8.483E-03	1.319E-02[a]	1.949E-02	2.313E-02	2.584E-02
	(...)	(...)	(...)	(...)	(5.968E-04)	(1.067E-03)	(1.531E-03)	(5.469E-04)	(3.646E-03)	(9.129E-05)	(1.236E-04)	(1.211E-04)
MCG +07-23-019	...	...	4.708E-04	7.601E-04	...	5.861E-03	8.472E-03	8.801E-03	1.542E-02	1.508E-02	1.931E-02	1.971E-02
	(...)	(...)	(5.812E-05)	(4.291E-05)	(...)	(3.239E-04)	(4.682E-04)	(5.674E-04)	(8.520E-04)	(6.866E-05)	(1.031E-04)	(8.964E-05)
CGCG 011-076	...	...	4.537E-05	1.541E-04	...	3.311E-03	7.112E-03	9.921E-03	1.871E-02	3.645E-02	4.807E-02	4.524E-02
	(...)	(...)	(7.689E-06)	(9.824E-06)	(...)	(1.220E-04)	(1.965E-04)	(6.396E-04)	(5.169E-04)	(6.378E-04)	(9.741E-04)	(1.208E-03)
IC 2810	...	...	1.164E-04	3.110E-04	...	4.325E-03	9.036E-03	2.151E-02	1.837E-02	3.454E-02	4.451E-02	3.866E-02
	(...)	(...)	(1.437E-05)	(1.756E-05)	(...)	(5.179E-04)	(1.082E-03)	(1.387E-03)	(2.030E-03)	(8.969E-05)	(1.505E-04)	(1.220E-04)
NGC 3690/IC 694	5.830E-08	2.047E-07	8.798E-03	1.373E-02	...	4.966E-02	7.244E-02	7.056E-02	1.294E-01	2.170E-01	3.064E-01	2.810E-01
	(...)	(...)	(1.086E-03)	(7.750E-04)	(...)	(9.148E-04)	(1.334E-03)	(4.549E-03)	(2.384E-03)	(2.525E-04)	(3.995E-04)	(3.149E-04)
IRAS F12112+0305	1.994E-09	3.112E-09	...	...	8.318E-04[b]	8.250E-04[b]	1.133E-03	2.211E-03	2.398E-03[b]	4.835E-03	5.941E-03	5.278E-03
	(...)	(...)	(...)	(...)	(1.532E-04)	(1.520E-05)	(3.132E-04)	(1.425E-04)	(2.398E-05)	(5.406E-05)	(6.844E-05)	(8.116E-05)
IRAS F12224-0624	...	...	...	...	...	8.166E-04	1.660E-03	3.024E-03	3.162E-03	5.045E-03	6.431E-03	5.474E-03
	(...)	(...)	(...)	(...)	(...)	(4.513E-05)	(7.643E-05)	(1.950E-04)	(1.165E-04)	(4.507E-04)	(4.620E-04)	(5.950E-04)
UGC 08058	4.691E-08	2.928E-08	...	...	7.586E-03[b]	1.202E-02[b]	1.282E-02[a]	1.616E-02	2.585E-02	6.412E-02	1.147E-01	1.991E-01
	(...)	(...)	(...)	(...)	(1.397E-03)	(2.215E-03)	(2.008E-03)	(1.042E-03)	(1.190E-02)	(1.214E-04)	(1.747E-04)	(1.944E-04)
NGC 4922	...	...	1.076E-04	3.586E-04	...	1.213E-02	2.377E-02	...	1.038E-01	7.266E-02	9.356E-02	7.761E-02
	(...)	(...)	(3.845E-06)	(3.275E-06)	(...)	(4.470E-04)	(8.757E-04)	(...)	(2.867E-03)	(1.205E-03)	(1.982E-03)	(1.859E-03)
ESO 507-G070	...	...	1.360E-04	2.331E-04	...	4.571E-03	9.204E-03	1.558E-02[a]	2.148E-02	4.512E-02	6.025E-02	5.426E-02
	(...)	(...)	(1.679E-05)	(1.316E-05)	(...)	(3.368E-04)	(5.087E-04)	(1.291E-03)	(1.187E-03)	(1.472E-04)	(2.671E-04)	(2.081E-04)
IC 0860	...	...	...	...	...	6.368E-03	1.180E-02	1.740E-02	2.228E-02	3.778E-02	4.856E-02	3.865E-02
	(...)	(...)	(...)	(...)	(...)	(1.760E-04)	(3.261E-04)	(1.122E-03)	(4.105E-04)	(6.264E-04)	(8.946E-04)	(9.967E-04)
VV 250a	8.933E-09	1.825E-08	6.253E-04	1.051E-03	...	6.310E-03	8.954E-03	...	1.486E-02	2.408E-02	3.223E-02	...
	(...)	(...)	(7.719E-05)	(5.931E-05)	(...)	(5.811E-04)	(6.597E-04)	(...)	(8.212E-04)	(8.872E-05)	(1.484E-04)	(...)
UGC 08387	3.049E-09	1.235-08	3.117E-04	6.781E-04	...	6.792E-03	9.908E-03	1.068E-02	1.941E-02	3.084E-02	3.846E-02	3.581E-02
	(...)	(...)	(3.847E-05)	(3.829E-05)	(...)	(3.128E-04)	(2.738E-04)	(6.885E-04)	(5.363E-04)	(1.035E-04)	(1.231E-04)	(1.431E-04)
NGC 5104	...	...	2.284E-04	4.732E-04	...	7.727E-03	1.500E-02	...	3.631E-02	7.153E-02	8.935E-02	8.440E-02
	(...)	(...)	(1.538E-05)	(1.637E-05)	(...)	(2.135E-04)	(4.144E-04)	(...)	(1.003E-03)	(1.976E-03)	(2.963E-03)	(2.177E-03)
MCG -03-34-064	1.448E-07[a]	1.192E-07[a]	2.337E-04	4.011E-04	...	1.330E-02	2.704E-02	...	5.702E-02	7.650E-02	9.689E-02	8.401E-02
	(...)	(...)	(2.307E-05)	(1.637E-05)	(...)	(1.470E-03)	(2.989E-03)	(...)	(6.302E-03)	(1.409E-03)	(1.785E-03)	(2.089E-03)
NGC 5135	3.840E-08[a]	1.775E-07[a]	1.384E-03	3.209E-03	2.070E-02[a]	2.858E-02	5.445E-02	...	1.202E-01	1.797E-01	2.615E-01	1.959E-01
	(...)	(...)	(4.613E-05)	(3.275E-05)	(2.669E-03)	(7.896E-04)	(1.505E-03)	(...)	(2.215E-03)	(3.641E-03)	(5.058E-03)	(5.772E-03)
NGC 5256	2.483E-08[a]	9.934E-09[a]	8.090E-04	1.419E-03	...	1.038E-02	1.871E-02	2.538E-02[a]	3.311E-02	5.266E-02	6.512E-02	6.266E-02
	(...)	(...)	(9.987E-05)	(8.014E-05)	(...)	(1.911E-04)	(3.446E-04)	(4.676E-04)	(6.100E-04)	(1.486E-04)	(2.356E-04)	(2.117E-04)
NGC 5257/8	...	...	3.319E-03	5.743E-03	...	2.679E-02	4.325E-02	5.978E-02	7.447E-02	1.314E-01	1.680E-01	1.477E-01
	(...)	(...)	(4.097E-04)	(3.243E-04)	(...)	(2.961E-03)	(4.780E-03)	(3.854E-03)	(8.231E-03)	(2.502E-04)	(3.197E-04)	(3.580E-04)
UGC 08696	4.815E-08	2.866E-07	2.039E-04	4.057E-04	3.020E-03[b]	5.297E-03[b]	9.036E-03	9.301E-03	1.380E-02[b]	3.042E-02	3.385E-02	3.581E-02
	(...)	(...)	(2.517E-05)	(2.291E-05)	(5.563E-04)	(3.415E-04)	(2.497E-03)	(5.997E-04)	(8.900E-04)	(1.055E-04)	(1.462E-04)	(1.410E-04)
CGCG 247-020	...	...	3.591E-05	5.878E-05	...	1.941E-03	3.664E-03	...	7.727E-03	1.518E-02	2.097E-02	2.010E-02
	(...)	(...)	(1.538E-05)	(1.146E-05)	(...)	(7.150E-05)	(4.388E-04)	(...)	(7.828E-04)	(4.754E-04)	(7.145E-04)	(8.144E-04)
IRAS F14348-1447	2.886E-09	5.359E-09	6.417E-05	1.288E-04	5.754E-04[b]	7.922E-04[b]	1.265E-03	2.424E-03	3.217E-03[b]	5.621E-03	7.847E-03	9.000E-03
	(...)	(...)	(7.921E-06)	(7.274E-06)	(1.060E-04)	(1.678E-05)	(3.495E-04)	(1.563E-04)	(5.926E-05)	(5.092E-05)	(7.111E-05)	(8.989E-05)

Table 4
(Continued)

RBGS Name	HX	SX	FUV	NUV	*U*	*B*	*V*	*R*	*I*	*J*	*H*	K_s
	2–10 KeV	0.5–2 KeV	152.8 Å	227.1 Å	3655 Å	4582 Å	5377 Å	6484 Å	8570 Å	1.241 μm	1.651 μm	2.165 μm
(1)	(2)	(3)	(4)	(5)	(6)	(7)	(8)	(9)	(10)	(11)	(12)	(13)
VV 340a	7.015E-09	1.684E-08	4.185E-04	7.972E-04	...	7.112E-03	1.406E-02	1.369E-02	2.679E-02	6.066E-02	9.391E-02	7.571E-02
	(...)	(...)	(5.166E-05)	(4.501E-05)	(...)	(7.861E-04)	(1.554E-03)	(8.829E-04)	(2.961E-03)	(1.117E-04)	(2.595E-04)	(2.092E-04)
CGCG 049-057	...	...	6.051E-05	1.524E-04	...	2.228E-03	4.786E-03	...	1.086E-02	2.140E-02	2.875E-02	2.366E-02
	(...)	(...)	(1.538E-06)	(1.474E-05)	(...)	(8.210E-05)	(1.763E-04)	(...)	(3.002E-04)	(6.703E-04)	(8.210E-04)	(1.002E-03)
VV 705	1.308E-09	9.917E-09	3.411E-04	6.693E-04	...	4.325E-03	6.368E-03	9.651E-03	1.247E-02	1.907E-02	2.473E-02	2.244E-02
	(...)	(...)	(4.210E-05)	(3.779E-05)	(...)	(1.992E-04)	(1.760E-04)	(6.222E-04)	(3.447E-04)	(8.558E-05)	(1.259E-04)	(1.190E-04)
IRAS F15250+3608	4.020E-10	2.660E-09	...	...	1.096E-03[b]	1.247E-03	1.905E-03	2.707E-03	2.606E-03	5.308E-03	7.152E-03	6.044E-03
	(...)	(...)	(...)	(...)	(2.020E-04)	(5.744E-05)	(8.775E-05)	(1.746E-04)	(3.529E-04)	(4.821E-05)	(7.816E-05)	(7.617E-05)
UGC 09913	5.073E-09	7.164E-09	1.313E-04	4.371E-04	6.076E-03[a]	9.272E-03[b]	1.893E-02[a]	2.131E-02	3.619E-02[b]	7.260E-02	8.793E-02	9.187E-02
	(...)	(...)	(1.620E-05)	(2.468E-05)	(1.287E-04)	(1.708E-04)	(3.261E-04)	(1.374E-03)	(3.333E-04)	(1.669E-04)	(2.400E-04)	(2.459E-04)
NGC 6090	...	...	1.094E-03	1.915E-03	...	7.379E-03	1.057E-02	1.789E-02	1.820E-02	2.933E-02	3.433E-02	3.492E-02
	(...)	(...)	(1.350E-04)	(1.081E-04)	(...)	(6.796E-04)	(5.840E-04)	(1.153E-03)	(5.028E-04)	(1.180E-04)	(1.637E-04)	(1.673E-04)
CGCG 052-037	...	...	1.192E-04	3.029E-04	...	4.966E-03	8.790E-03	1.344E-02	1.854E-02	3.655E-02	4.583E-02	4.516E-02
	(...)	(...)	(1.538E-05)	(1.474E-05)	(...)	(1.372E-04)	(3.238E-04)	(8.668E-04)	(5.121E-04)	(7.069E-04)	(1.266E-04)	(1.206E-03)
NGC 6286	...	...	5.628E-04	1.058E-03	...	1.542E-02	2.443E-02	6.260E-02	5.058E-02	5.687E-02	8.224E-02	8.301E-02
	(...)	(...)	(2.307E-05)	(1.637E-05)	(...)	(1.988E-03)	(3.151E-03)	(4.036E-03)	(6.056E-03)	(8.381E-04)	(1.363E-03)	(3.364E-03)
IRAS F17132+5313	9.210E-10	4.268E-09	3.538E-05	9.769E-05	...	7.311E-04	1.486E-03	2.941E-03	2.679E-03	1.168E-02	1.593E-02	1.576E-02
	(...)	(...)	(4.367E-06)	(5.515E-06)	(...)	(3.367E-05)	(5.474E-05)	(1.896E-04)	(9.870E-05)	(5.672E-05)	(7.121E-05)	(7.730E-05)
ESO 602-G025	...	...	2.791E-04	5.534E-04	...	6.668E-03	1.159E-02	1.772E-02	2.400E-02	4.930E-02	6.419E-02	5.785E-02
	(...)	(...)	(3.076E-05)	(3.275E-05)	(...)	(1.842E-04)	(3.202E-04)	(1.143E-03)	(1.547E-03)	(1.135E-03)	(1.774E-03)	(1.865E-03)
IRAS F22491-1808	2.807E-10	2.920E-09	1.673E-04	2.348E-04	4.365E-04[b]	9.543E-04[b]	8.551E-04	2.131E-03	2.399E-03[b]	3.972E-03	4.923E-03	4.808E-03
	(...)	(...)	(2.066E-05)	(1.326E-05)	(8.041E-05)	(1.758E-05)	(1.575E-04)	(1.374E-04)	(1.547E-04)	(3.651E-05)	(5.112E-05)	(5.686E-05)
NGC 7469	1.906E-06[a]	...	4.322E-03	5.948E-03	3.020E-02[b]	2.890E-02	4.713E-02	6.202E-02	9.290E-02	1.915E-01	2.369E-01	2.356E-01
	(...)	(...)	(5.335E-04)	(3.358E-04)	(5.563E-03)	(1.863E-03)	(2.605E-03)	(3.999E-03)	(3.422E-03)	(2.486E-04)	(3.390E-04)	(3.269E-04)
CGCG 453-062	...	...	5.774E-05	2.112E-04	...	3.436E-03	6.427E-03	...	1.330E-02	3.219E-02	4.111E-02	3.861E-02
	(...)	(...)	(1.538E-05)	(1.474E-05)	(...)	(1.266E-04)	(1.776E-04)	(...)	(3.676E-04)	(6.522E-04)	(8.708E-04)	(1.174E-03)
IC 5298	...	...	1.220E-04	2.934E-04	...	3.597E-03	8.166E-03	1.182E-02	1.854E-02	3.481E-02	4.963E-02	4.860E-02
	(...)	(...)	(1.506E-05)	(1.656E-05)	(...)	(1.325E-04)	(2.256E-04)	(7.619E-04)	(6.829E-04)	(1.130E-04)	(1.563E-04)	(1.678E-04)
NGC 7592	...	...	1.784E-03	2.259E-03	...	9.638E-03	1.393E-02	1.926E-02	2.606E-02	4.509E-02	5.325E-02	3.351E-02
	(...)	(...)	(4.613E-05)	(3.275E-05)	(...)	(3.551E-04)	(3.849E-04)	(1.241E-03)	(7.201E-04)	(6.645E-04)	(1.275E-03)	(1.142E-03)
NGC 7674	4.828E-08[a]	7.430E-08[a]	1.325E-03	1.937E-03	9.638E-03[a]	1.228E-02	2.109E-02	3.196E-02	3.908E-02	7.315E-02	1.114E-01	8.746E-02
	(...)	(...)	(1.636E-04)	(1.094E-04)	(9.765E-04)	(6.783E-04)	(5.826E-04)	(2.060E-03)	(7.200E-04)	(1.672E-04)	(2.620E-04)	(2.150E-04)
NGC 7770/1	...	...	2.607E-03	3.848E-03	1.419E-02[a]	3.076E-02	6.194E-02	9.562E-02	1.486E-01	2.609E-01	3.335E-01	3.053E-01
	(...)	(...)	(6.151E-06)	(3.275E-06)	(1.307E-03)	(8.500E-04)	(1.141E-03)	(6.165E-03)	(2.737E-03)	(2.643E-03)	(4.300E-03)	(4.780E-03)
MRK 0331	...	4.000E-08[a]	6.128E-05	2.691E-04	...	5.740E-03	1.110E-02	1.732E-02	2.584E-02	6.500E-02	8.684E-02	8.355E-02
	(...)	(...)	(4.215E-06)	(8.629E-06)	(...)	(4.170E-04)	(8.060E-04)	(1.117E-03)	(7.650E-04)	(1.197E-04)	(1.600E-04)	(1.539E-04)

Notes. The photometry values have been measured with a uniform mask for each object. Exceptions in each column are marked by superscripted letters indicating literature or NED reference. Uncertainty values are indicated in parantheses where available. Columns 2 and 3: X-ray *Chandra*-ACIS photometry (Iwasawa et al. 2011). Columns 4 and 5: NUV–FUV *GALEX* photometry measured from image data in Howell et al. (2010). Column 6: UV photometry from Surace et al. (2000) and this paper. Columns 7 and 8: *B*- and *V*-band photometry from Ishida (2004), Surace et al. (1998), and Surace & Sanders (2000). Column 9: *R*-band photometry from J. M. Mazzarella et al. (2012, in preparation). Column 10: *I*-band photometry from Ishida (2004), Surace et al. (1998), and Surace & Sanders (2000). Columns 11–13: *J*, *H*, K_s photometry from 2MASS.

[a] NED.

[b] Surace et al. (1998, 2000) and Surace & Sanders (2000).

Table 5
Local (U)LIRG Photometry (Jy; $\lambda > 3\,\mu$m)

Object	IRAC1 3.6 μm	IRAC2 4.5 μm	IRAC3 5.8 μm	IRAC4 8.0 μm	IRAS1 12 μm	MIPS1 24 μm	IRAS2 25 μm	IRAS3 60 μm	MIPS2 70 μm	IRAS4 100 μm	MIPS3 160 μm	SCUBA1 450 μm	SCUBA2 850 μm	VLA1 4.85 GHz	VLA2 1.49 GHz
(1)	(2)	(3)	(4)	(5)	(6)	(7)	(8)	(9)	(10)	(11)	(12)	(13)	(14)	(15)	(16)
NGC 0034	0.050	0.053	0.119	0.314	0.350	1.999	2.390	17.050	13.285	16.860	12.867	...	...	...	0.061
	(0.005)	(0.005)	(0.005)	(0.005)	(0.032)	(0.100)	(0.055)	(0.045)	(1.993)	(0.135)	(3.860)	(...)	(...)	(...)	(0.001)
MCG -02-01-051/2	0.040	0.029	0.081	0.225	0.280	1.120	1.200	7.480	7.472	9.660	9.120	...	...	...	0.041
	(0.004)	(0.003)	(0.004)	(0.004)	(0.034)	(0.056)	(0.055)	(0.048)	(1.121)	(0.138)	(2.736)	(...)	(...)	(...)	(0.001)
NGC 0232	0.098	0.071	0.129	0.276	0.360	1.223	1.280	10.050	12.341	17.140	16.965	...	...	...	0.052
	(0.010)	(0.007)	(0.010)	(0.010)	(0.034)	(0.061)	(0.039)	(0.037)	(1.851)	(0.094)	(5.090)	(...)	(...)	(...)	(0.001)
IC 1623A/B	0.092	0.099	0.241	0.542	1.030	3.014	3.650	22.930	...	31.550	...	...	...	0.096	0.221
	(0.009)	(0.010)	(0.009)	(0.009)	(0.030)	(0.151)	(0.050)	(0.062)	(...)	(0.113)	(...)	(...)	(...)	(0.012)	(0.001)
MCG -03-04-014	0.032	0.023	0.072	0.209	0.340	0.742	0.900	7.250	7.440	10.330	9.626	...	...	...	0.040
	(0.003)	(0.002)	(0.003)	(0.003)	(0.043)	(0.037)	(0.036)	(0.060)	(1.116)	(0.136)	(2.888)	(...)	(...)	(...)	(0.001)
CGCG 436-030	0.044	0.039	0.080	0.174	0.210	1.230	1.540	10.710	8.711	9.670	6.828	...	0.039	...	0.049
	(0.004)	(0.004)	(0.004)	(0.004)	(0.043)	(0.062)	(0.048)	(0.038)	(1.307)	(0.188)	(2.048)	(...)	(0.008)	(...)	(0.001)
IRAS F01364-1042	0.003	0.004	0.007	0.021	<0.16	0.255	0.440	6.620	5.986	6.880	3.660	...	...	0.012	0.015
	(0.000)	(0.000)	(0.000)	(0.000)	(...)	(0.013)	(0.036)	(0.042)	(0.898)	(0.114)	(1.098)	(...)	(...)	(...)	(0.001)
III Zw 035	0.018	0.013	0.026	0.062	<0.06	0.761	1.030	13.250	10.962	14.300	7.317	...	0.076	...	0.041
	(0.002)	(0.001)	(0.002)	(0.002)	(...)	(0.038)	(0.059)	(0.050)	(1.644)	(0.155)	(2.195)	(...)	(0.015)	(...)	(0.001)
NGC 0695	0.058	0.042	0.125	0.362	0.500	0.722	0.830	7.590	8.828	13.560	11.200	...	0.136	...	0.066
	(0.006)	(0.004)	(0.006)	(0.006)	(0.023)	(0.036)	(0.041)	(0.031)	(1.324)	(0.167)	(3.360)	(...)	(0.021)	(...)	(0.001)
NGC 0958	0.128	0.082	0.189	0.421	0.620	0.516	0.940	5.850	7.846	15.080	19.138	2.251	0.262	...	0.058
	(0.013)	(0.008)	(0.013)	(0.013)	(0.030)	(0.026)	(0.035)	(0.040)	(1.177)	(0.198)	(5.741)	(0.428)	(0.034)	(...)	(0.001)
UGC 02238	0.050	0.038	0.142	0.383	0.360	0.524	0.650	8.170	9.526	15.670	13.240	...	0.104	...	0.067
	(0.005)	(0.004)	(0.005)	(0.005)	(0.030)	(0.026)	(0.042)	(0.036)	(1.429)	(0.128)	(3.972)	(...)	(0.014)	(...)	(0.001)
UGC 02369	0.042	0.030	0.063	0.149	0.230	1.160	1.880	8.070	7.823	11.180	8.717	0.523	0.072	...	0.050
	(0.004)	(0.003)	(0.004)	(0.004)	(0.022)	(0.058)	(0.042)	(0.043)	(1.173)	(0.190)	(2.615)	(0.120)	(0.013)	(...)	(0.001)
IRAS F03359+1523	0.010	0.008	0.020	0.053	<0.07	0.428	0.650	5.970	6.409	7.270	3.652	...	0.044	...	0.019
	(0.001)	(0.001)	(0.001)	(0.001)	(...)	(0.021)	(0.043)	(0.041)	(0.961)	(0.128)	(1.096)	(...)	(0.009)	(...)	(0.001)
UGC 02982	0.076	0.053	0.186	0.481	0.570	0.673	0.830	8.390	9.862	16.820	15.831	...	0.176	...	0.082
	(0.008)	(0.005)	(0.008)	(0.008)	(0.014)	(0.034)	(0.019)	(0.043)	(1.479)	(0.287)	(4.749)	(...)	(0.034)	(...)	(0.001)
ESO 550-IG025	0.029	0.021	0.045	0.131	0.220	0.392	0.510	5.690	6.456	9.470	7.724	...	...	...	0.038
	(0.003)	(0.002)	(0.003)	(0.003)	(0.024)	(0.020)	(0.034)	(0.030)	(0.968)	(0.115)	(2.317)	(...)	(...)	(...)	(0.001)
NGC 1614	0.101	0.076	0.279	0.742	1.380	6.552	7.500	32.120	26.535	34.320	18.674	0.981	0.140	0.063	0.123
	(0.010)	(0.008)	(0.010)	(0.010)	(0.023)	(0.328)	(0.025)	(0.083)	(3.980)	(0.430)	(5.602)	(0.167)	(0.020)	(...)	(0.001)
IRAS F05189-2524	0.100	0.129	0.227	0.290	0.740	2.546	3.470	13.250	...	11.840	...	...	...	...	0.028
	(0.010)	(0.013)	(0.010)	(0.010)	(0.016)	(0.127)	(0.018)	(0.029)	(...)	(0.077)	(...)	(...)	(...)	(...)	(0.001)
NGC 2623	0.031	0.027	0.056	0.140	0.210	1.399	1.810	23.740	20.912	25.880	14.424	...	0.091	0.057	0.099
	(0.003)	(0.003)	(0.003)	(0.003)	(0.023)	(0.070)	(0.041)	(0.028)	(3.137)	(0.111)	(4.327)	(...)	(0.014)	(0.009)	(0.001)
IRAS F08572+3915	0.041	0.101	0.297	0.314	0.330	1.444	1.760	7.300	5.613	4.770	2.442	...	0.017	...	0.005
	(0.004)	(0.004)	(0.004)	(0.004)	(0.031)	(0.072)	(0.033)	(0.028)	(0.842)	(0.152)	(0.733)	(...)	(0.007)	(...)	(0.001)
UGC 04881	0.017	0.009	0.008	0.004	0.140	0.435	0.610	6.070	6.995	10.330	8.447	...	0.065	...	0.032
	(0.002)	(0.001)	(0.002)	(0.002)	(0.037)	(0.022)	(0.034)	(0.048)	(1.049)	(0.109)	(2.534)	(...)	(0.013)	(...)	(0.001)
UGC 05101	0.046	0.078	0.096	0.144	0.250	0.808	1.020	11.680	13.195	19.910	13.393	...	...	0.076	0.150
	(0.005)	(0.008)	(0.005)	(0.005)	(0.027)	(0.040)	(0.027)	(0.034)	(1.979)	(0.137)	(4.018)	(...)	(...)	(0.011)	(0.001)
MCG +08-18-013	0.024	0.017	0.047	0.126	0.100	0.587	0.750	5.680	7.316	8.420	6.722	...	0.042	...	0.022
	(0.002)	(0.002)	(0.002)	(0.002)	(0.019)	(0.029)	(0.028)	(0.028)	(1.097)	(0.143)	(2.017)	(...)	(0.010)	(...)	(0.001)
IC 0563/4	0.069	0.046	0.123	0.307	0.460	0.490	0.540	5.260	7.237	12.180	18.104	...	0.228	...	0.060
	(0.007)	(0.005)	(0.007)	(0.007)	(0.021)	(0.025)	(0.039)	(0.026)	(1.086)	(0.058)	(5.431)	(...)	(0.035)	(...)	(0.001)

Table 5
(Continued)

Object	IRAC1 3.6 μm	IRAC2 4.5 μm	IRAC3 5.8 μm	IRAC4 8.0 μm	IRAS1 12 μm	MIPS1 24 μm	IRAS2 25 μm	IRAS3 60 μm	MIPS2 70 μm	IRAS4 100 μm	MIPS3 160 μm	SCUBA1 450 μm	SCUBA2 850 μm	VLA1 4.85 GHz	VLA2 1.49 GHz
(1)	(2)	(3)	(4)	(5)	(6)	(7)	(8)	(9)	(10)	(11)	(12)	(13)	(14)	(15)	(16)
NGC 3110	0.101	0.069	0.219	0.555	0.590	1.016	1.130	11.280	11.779	22.270	17.168	...	0.188	...	0.109
	(0.010)	(0.007)	(0.010)	(0.010)	(0.035)	(0.051)	(0.048)	(0.033)	(1.767)	(0.085)	(5.150)	(...)	(0.028)	(...)	(0.001)
IRAS F10173+0828	0.011	0.006	0.013	0.014	0.190	0.276	0.550	5.610	5.241	5.860	3.264	...	0.036	...	0.009
	(0.001)	(0.001)	(0.001)	(0.001)	(0.029)	(0.014)	(0.049)	(0.025)	(0.786)	(0.100)	(0.979)	(...)	(0.006)	(...)	(0.001)
IRAS F10565+2448	0.021	0.018	0.039	0.127	0.200	0.976	1.270	12.100	11.259	15.010	9.174	0.533	0.061	...	0.051
	(0.002)	(0.002)	(0.002)	(0.002)	(0.030)	(0.049)	(0.031)	(0.025)	(1.689)	(0.122)	(2.752)	(...)	(0.013)	(...)	(0.001)
MCG +07-23-019	0.016	0.012	0.034	0.093	0.200	0.245	0.710	6.380	7.172	10.300	7.284	0.646	0.092	...	0.031
	(0.002)	(0.001)	(0.002)	(0.002)	(0.019)	(0.012)	(0.022)	(0.034)	(1.076)	(0.106)	(2.185)	(0.156)	(0.020)	(...)	(0.001)
CGCG 011-076	0.040	0.034	0.075	0.192	0.480	0.680	0.760	5.850	6.328	9.180	8.364	0.571	0.084	...	0.032
	(0.004)	(0.003)	(0.004)	(0.004)	(0.039)	(0.034)	(0.050)	(0.057)	(0.949)	(0.253)	(2.509)	(0.166)	(0.013)	(...)	(0.001)
IC 2810	0.026	0.019	0.047	0.113	0.140	0.492	0.620	6.200	8.771	10.390	12.389	...	0.106	...	0.026
	(0.003)	(0.002)	(0.003)	(0.003)	(0.034)	(0.025)	(0.062)	(0.038)	(1.316)	(0.136)	(3.717)	(...)	(0.018)	(...)	(0.001)
NGC 3690/IC 694	0.313	0.340	1.049	2.157	3.970	...	24.510	113.050	79.355	111.420	...	...	...	...	0.658
	(0.031)	(0.034)	(0.031)	(0.031)	(0.020)	(...)	(0.031)	(0.052)	(11.903)	(0.133)	(...)	(...)	(...)	(...)	(0.001)
IRAS F12112+0305	0.009	0.006	0.009	0.050	<0.11	0.364	0.660	8.180	...	9.460	...	0.429	0.049	...	0.024
	(0.001)	(0.001)	(0.001)	(0.001)	(...)	(0.018)	(0.054)	(0.032)	(...)	(0.123)	(...)	(...)	(0.010)	(...)	(0.001)
IRAS F12224-0624	0.007	0.004	0.008	0.016	<0.11	0.159	0.200	5.990	5.832	8.130	4.798	...	0.074	...	0.009
	(0.001)	(0.000)	(0.001)	(0.001)	(...)	(0.008)	(0.044)	(0.044)	(0.875)	(0.139)	(1.439)	(...)	(0.015)	(...)	(0.001)
UGC 08058	0.206	0.280	1.394	0.907	1.830	4.337	8.840	30.800	...	29.740	...	...	...	0.414	0.296
	(0.021)	(0.028)	(0.021)	(0.021)	(0.017)	(0.217)	(0.028)	(0.042)	(...)	(0.108)	(...)	(...)	(...)	(0.062)	(0.001)
NGC 4922	0.059	0.051	0.068	0.132	0.270	1.171	1.480	6.210	5.740	7.330	5.256	...	0.053	...	0.038
	(0.006)	(0.005)	(0.006)	(0.006)	(0.035)	(0.059)	(0.030)	(0.040)	(0.861)	(0.093)	(1.577)	(...)	(0.012)	(...)	(0.001)
ESO 507-G070	0.037	0.026	0.047	0.099	0.250	0.643	0.800	13.040	13.102	15.710	9.489	...	...	...	0.060[a]
	(0.004)	(0.003)	(0.004)	(0.004)	(0.020)	(0.032)	(0.046)	(0.051)	(1.965)	(0.159)	(2.847)	(...)			
IC 0860	0.023	0.014	0.018	0.036	<0.14	0.901	1.340	18.610	15.379	18.660	9.336	...	0.118	...	0.033
	(0.002)	(0.001)	(0.002)	(0.002)	(...)	(0.045)	(0.044)	(0.071)	(2.307)	(0.900)	(2.801)	(...)	(0.020)	(...)	(0.001)
VV 250a	0.033	0.026	0.085	0.213	0.350	...	1.950	11.390	...	12.410	...	...	...	...	0.050
	(0.003)	(0.003)	(0.003)	(0.003)	(0.022)	(...)	(0.020)	(0.035)	(...)	(0.093)	(...)	(...)	(...)	(...)	(0.001)
UGC 08387	0.032	0.025	0.083	0.219	0.250	1.070	1.420	17.040	17.681	24.380	14.213	...	0.113	0.053	0.101
	(0.003)	(0.003)	(0.003)	(0.003)	(0.029)	(0.054)	(0.040)	(0.088)	(2.652)	(0.120)	(4.264)	(...)	(0.015)	(0.008)	(0.001)
NGC 5104	0.055	0.038	0.076	0.179	0.390	0.554	0.740	6.780	7.461	13.370	11.508	...	0.091	...	0.035
	(0.006)	(0.004)	(0.006)	(0.006)	(0.034)	(0.028)	(0.091)	(0.049)	(1.119)	(0.103)	(3.452)	(...)	(0.020)	(...)	(0.001)
MCG -03-34-064	0.093	0.105	0.214	0.328	0.940	2.253	2.970	6.200	1.292	6.200	2.499	...	...	...	0.267[a]
	(0.009)	(0.011)	(0.009)	(0.009)	(0.040)	(0.113)	(0.045)	(0.040)	(0.194)	(0.143)	(0.750)	(...)	(...)	(...)	(...)
NGC 5135	0.132	0.104	0.220	0.459	0.630	...	2.380	16.860	...	30.970	23.012	...	...	...	0.194[a]
	(0.013)	(0.010)	(0.013)	(0.013)	(0.035)	(...)	(0.058)	(0.046)	(...)	(0.177)	(6.904)	(...)	(...)	(...)	(...)
NGC 5256	0.043	0.033	0.067	0.161	0.320	0.873	1.070	7.250	7.746	10.110	7.021	...	0.082	0.047	0.113
	(0.004)	(0.003)	(0.004)	(0.004)	(0.018)	(0.044)	(0.028)	(0.033)	(1.162)	(0.135)	(2.106)	(...)	(0.017)	(0.007)	(0.001)
NGC 5257/8	0.088	0.060	0.171	0.441	0.570	1.180	1.340	10.730	14.015	19.970	22.598	...	0.283	...	0.076
	(0.009)	(0.006)	(0.009)	(0.009)	(0.031)	(0.059)	(0.069)	(0.059)	(2.102)	(0.050)	(6.779)	(...)	(0.039)	(...)	(0.001)
UGC 08696	0.032	0.039	0.073	0.143	0.240	1.864	2.360	22.510	20.206	22.530	11.661	...	...	0.099	0.143
	(0.003)	(0.004)	(0.003)	(0.003)	(0.017)	(0.093)	(0.021)	(0.042)	(3.031)	(0.070)	(3.498)	(...)	(...)	(0.015)	(0.001)
CGCG 247-020	0.017	0.013	0.034	0.088	0.150	0.705	0.840	6.010	6.222	8.470	5.403	0.284	0.036	...	0.021
	(0.002)	(0.001)	(0.002)	(0.002)	(0.022)	(0.035)	(0.019)	(0.035)	(0.933)	(0.155)	(1.621)	(0.111)	(0.008)	(...)	(0.001)
IRAS F14348-1447	0.012	0.011	0.011	0.049	<0.10	0.393	0.550	6.820	...	7.310	...	...	...	...	0.037
	(0.001)	(0.001)	(0.001)	(0.001)	(...)	(0.020)	(0.062)	(0.040)	(...)	(0.151)	(...)	(...)	(...)	(...)	(0.001)

Table 5
(Continued)

Object	IRAC1 3.6 μm	IRAC2 4.5 μm	IRAC3 5.8 μm	IRAC4 8.0 μm	IRAS1 12 μm	MIPS1 24 μm	IRAS2 25 μm	IRAS3 60 μm	MIPS2 70 μm	IRAS4 100 μm	MIPS3 160 μm	SCUBA1 450 μm	SCUBA2 850 μm	VLA1 4.85 GHz	VLA2 1.49 GHz
(1)	(2)	(3)	(4)	(5)	(6)	(7)	(8)	(9)	(10)	(11)	(12)	(13)	(14)	(15)	(16)
VV 340a	0.056	0.042	0.100	0.274	0.360	0.424	0.410	6.950	8.896	15.160	14.563	...	0.215	0.039	0.075
	(0.006)	(0.004)	(0.006)	(0.006)	(0.016)	(0.021)	(0.031)	(0.029)	(1.334)	(0.169)	(4.369)	(...)	(0.031)	(0.006)	(0.001)
CGCG 049-057	0.018	0.013	0.027	0.056	<0.05	0.555	0.950	21.890	20.487	31.530	...	...	0.200	...	0.046
	(0.002)	(0.001)	(0.002)	(0.002)	(...)	(0.028)	(0.029)	(0.072)	(3.073)	(0.158)	(...)	(...)	(0.027)	(...)	(0.001)
VV 705	0.028	0.022	0.065	0.130	0.290	1.196	1.420	9.020	8.479	10.000	6.308	0.423	0.060	0.031	0.048
	(0.003)	(0.002)	(0.003)	(0.003)	(0.019)	(0.060)	(0.016)	(0.021)	(1.272)	(0.091)	(1.892)	(0.093)	(0.014)	(0.005)	(0.001)
IRAS F15250+3608	0.010	0.010	0.038	0.122	0.160	1.065	1.310	7.100	6.309	5.930	3.214	0.252	0.033	...	0.014
	(0.001)	(0.001)	(0.001)	(0.001)	(0.030)	(0.053)	(0.025)	(0.043)	(0.946)	(0.098)	(0.964)	(0.070)	(0.008)	(...)	(0.001)
UGC 09913	0.054	0.045	0.137	0.251	0.610	4.010	8.000	104.090	80.771	115.290	...	...	0.832	0.208	0.324
	(0.005)	(0.005)	(0.005)	(0.005)	(0.021)	(0.201)	(0.034)	(0.112)	(12.116)	(0.138)	(...)	(...)	(0.086)	(0.031)	(0.001)
NGC 6090	0.033	0.023	0.061	0.177	0.260	0.954	1.240	6.480	6.762	9.410	7.233	...	...	...	0.046
	(0.003)	(0.002)	(0.003)	(0.003)	(0.020)	(0.048)	(0.021)	(0.030)	(1.014)	(0.102)	(2.170)	(...)	(...)	(...)	(0.001)
CGCG 052-037	0.041	0.030	0.082	0.222	0.250	0.786	0.810	7.000	7.559	11.230	9.288	...	0.095	...	0.031
	(0.004)	(0.003)	(0.004)	(0.004)	(0.030)	(0.039)	(0.031)	(0.022)	(1.134)	(0.133)	(2.786)	(...)	(0.018)	(...)	(0.001)
NGC 6286	0.065	0.047	0.134	0.329	0.470	0.581	0.620	9.240	13.129	23.110	21.270	...	...	...	0.156
	(0.007)	(0.005)	(0.007)	(0.007)	(0.015)	(0.029)	(0.017)	(0.043)	(1.969)	(0.048)	(6.381)	(...)	(...)	(...)	(0.001)
IRAS F17132+5313	0.017	0.014	0.030	0.105	0.240	0.493	0.650	6.070	6.115	7.900	5.576	...	...	...	0.026
	(0.002)	(0.001)	(0.002)	(0.002)	(0.021)	(0.025)	(0.024)	(0.034)	(0.917)	(0.105)	(1.673)	(...)	(...)	(...)	(0.001)
ESO 602-G025	0.043	0.037	0.098	0.229	0.270	0.608	0.910	5.420	6.359	9.640	7.844	...	...	...	0.041
	(0.004)	(0.004)	(0.004)	(0.004)	(0.029)	(0.030)	(0.045)	(0.044)	(0.954)	(0.082)	(2.353)	(...)	(...)	(...)	(0.001)
IRAS F22491-1808	0.009	0.004	0.003	0.028	<0.09	0.433	0.540	5.540	4.744	4.640	3.014	...	...	...	0.006
	(0.001)	(0.000)	(0.001)	(0.001)	(...)	(0.022)	(0.067)	(0.036)	(0.712)	(0.095)	(0.904)	(...)	(...)	(...)	(0.001)
NGC 7469	0.209	0.187	0.665	0.771	1.590	4.080	5.960	27.330	25.034	35.160	...	...	0.264	0.071	0.169
	(0.021)	(0.019)	(0.021)	(0.021)	(0.039)	(0.204)	(0.032)	(0.040)	(3.755)	(0.599)	(...)	(...)	(0.030)	(0.011)	(0.001)
CGCG 453-062	0.032	0.022	0.056	0.136	0.190	0.411	0.540	7.190	7.619	11.730	10.317	...	0.069	...	0.037
	(0.003)	(0.002)	(0.003)	(0.003)	(0.038)	(0.021)	(0.038)	(0.047)	(1.143)	(0.163)	(3.095)	(...)	(0.014)	(...)	(0.001)
IC 5298	0.037	0.045	0.048	0.132	0.340	1.427	1.950	9.060	8.424	11.990	6.774	...	0.077	...	0.034
	(0.004)	(0.005)	(0.004)	(0.004)	(0.024)	(0.071)	(0.053)	(0.051)	(1.264)	(0.097)	(2.032)	(...)	(0.015)	(...)	(0.001)
NGC 7592	0.044	0.037	0.091	0.214	0.260	0.868	0.970	8.050	7.445	10.580	8.833	...	0.108	...	0.062
	(0.004)	(0.004)	(0.004)	(0.004)	(0.031)	(0.043)	(0.056)	(0.049)	(1.117)	(0.137)	(2.650)	(...)	(0.019)	(...)	(0.001)
NGC 7674	0.090	0.093	0.202	0.295	0.680	1.600	1.920	5.360	5.881	8.330	7.966	...	0.108	0.086	0.209
	(0.009)	(0.009)	(0.009)	(0.009)	(0.037)	(0.080)	(0.034)	(0.042)	(0.882)	(0.141)	(2.390)	(...)	(0.020)	(0.013)	(0.001)
NGC 7770/1	0.321	0.213	0.447	0.958	0.990	1.773	2.170	19.670	23.341	40.120	...	...	0.377	...	0.124
	(0.032)	(0.021)	(0.032)	(0.032)	(0.036)	(0.089)	(0.036)	(0.135)	(3.501)	(0.839)	(...)	(...)	(0.042)	(...)	(0.001)
MRK 0331	0.054	0.039	0.133	0.320	0.520	...	2.540	18.000	...	22.700	...	...	0.132	0.028	0.068
	(0.005)	(0.004)	(0.005)	(0.005)	(0.035)	(...)	(0.026)	(0.046)	(...)	(0.194)	(...)	(...)	(0.025)	(0.006)	(0.001)

Notes. The photometry values have been measured with a uniform mask for each object. Exceptions in each column are marked by superscripted letters indicating literature or NED reference. Uncertainty values are indicated in parantheses where available.

Columns 2–5: *Spitzer*-IRAC photometry from images in J. M. Mazzarella et al. (2012, in preparation) and J. A. Surace (2012, in preparation).

Column 6: *IRAS* photometry from Sanders et al. (2003).

Column 7: *Spitzer*-MIPS24 photometry from images in J. M. Mazzarella et al. (2012, in preparation) and J. A. Surace (2012, in preparation).

Columns 8 and 9: *IRAS* photometry from Sanders et al. (2003).

Column 10: *Spitzer*-MIPS70 photometry from images in J. M. Mazzarella et al. (2012, in preparation) and J. A. Surace (2012, in preparation).

Column 11: *IRAS* photometry from Sanders et al. (2003).

Column 12: *Spitzer*-MIPS160 photometry from images in J. M. Mazzarella et al. (2012, in preparation) and J. A. Surace (2012, in preparation).

Columns 13 and 14: JCMT/SCUBA submillimeter photometry from Dunne et al. (2000) and Dunne & Eales (2001).

Columns 15 and 16: VLA photometry from Condon et al. (1990, 1991).

[a] At 1.425 GHz; photometry from Condon et al. (1996).

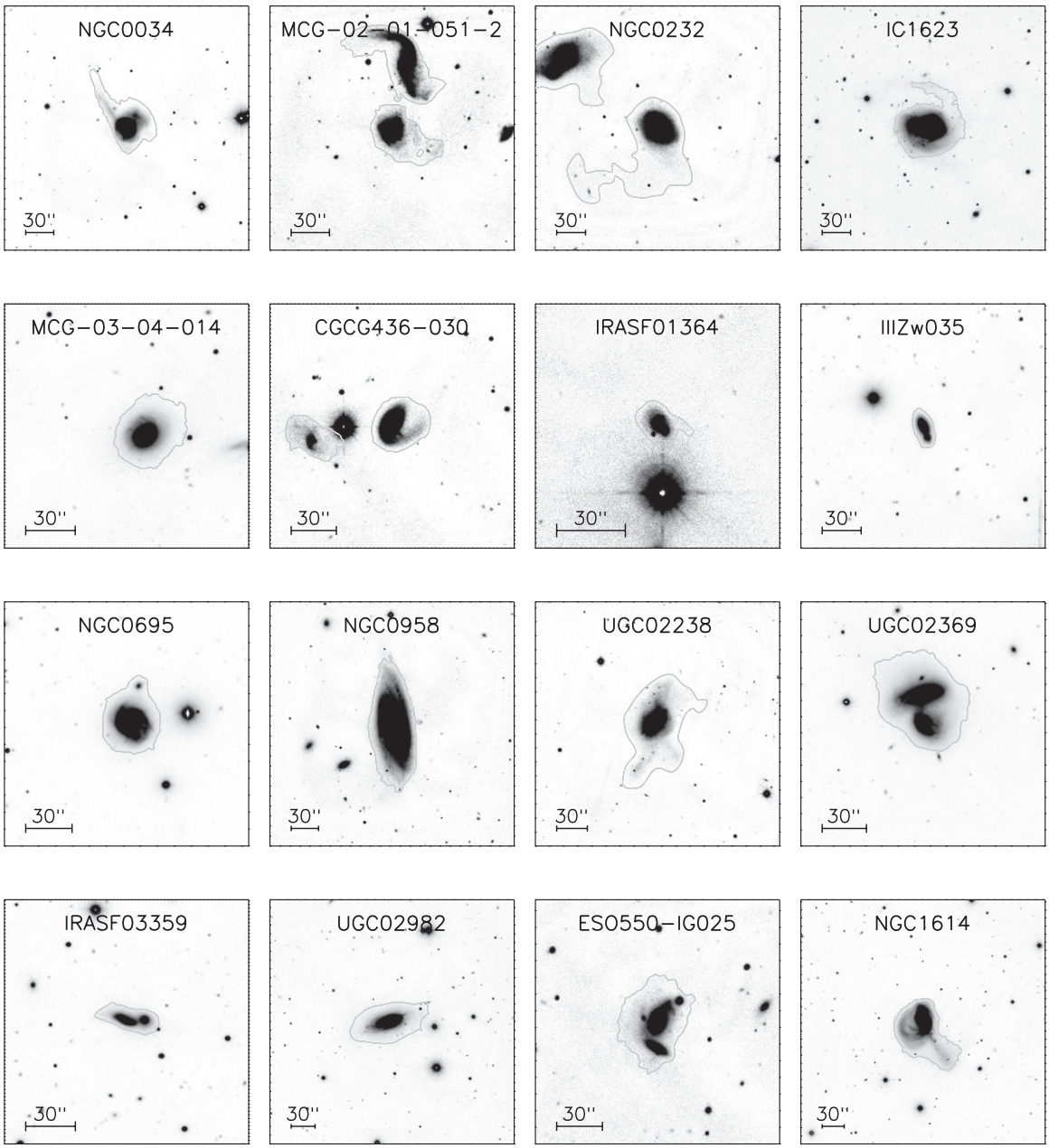

Figure 1. *HST* and UH 2.2 m *I*-band images in increasing R.A. order for the 64 local (U)LIRGs with mask photometry contour superimposed. The field of view for all images is 100 kpc × 100 kpc, and a 30″ scale bar is drawn inside each frame to help guide the eye.

separately. Qualitatively speaking, the overall SED shape is similar for all of the LIRGs and ULIRGs, with two significant maxima, one of which is near 1 μm and the other near 80 μm, with a large dip between them, and all SEDs falling toward the FUV and at submillimeter wavelengths. The logarithmic difference between the stellar and dust peaks is 1.2 dex for the ULIRGs but only 0.7 dex for the LIRGs, providing a quantitative measure for the change in stellar-to-dust ratio with infrared luminosity. The next two sections offer different ways to quantify the spectral shapes. The fit data values for the mean SEDs for both LIRGs and ULIRGs are given in Table 6.

4.2. Spectral Indices

A useful and more quantitative way of discussing the spectral shapes of SEDs makes use of spectral indices defined as follows:

$$\alpha_2^1 = \frac{\log \nu_1 f_{\nu_1} - \log \nu_2 f_{\nu_2}}{\log \nu_1 - \log \nu_2}, \quad (1)$$

where the indices (1 and 2) correspond to observed wavelengths in μm. To mirror a high-z SED study of a 70 μm selected sample of (U)LIRGs (Kartaltepe et al. 2010), here we have chosen three wavelength ranges where the SEDs appear to show the largest variations—in the UV–optical (0.23–0.54 μm), NIR (2.2–4.5 μm), and the MIR (8–24 μm). These three wavelength ranges correspond to the shaded regions shown in Figure 4. The top panels in Figure 5 show α_2^1 versus $L_{\rm IR}$ for three different spectral indices, corresponding to the three wavelength ranges described above. The mean values of α_2^1 for LIRGs and ULIRGs along with a regression analysis for the full subsample of 64 objects is given in Table 7.

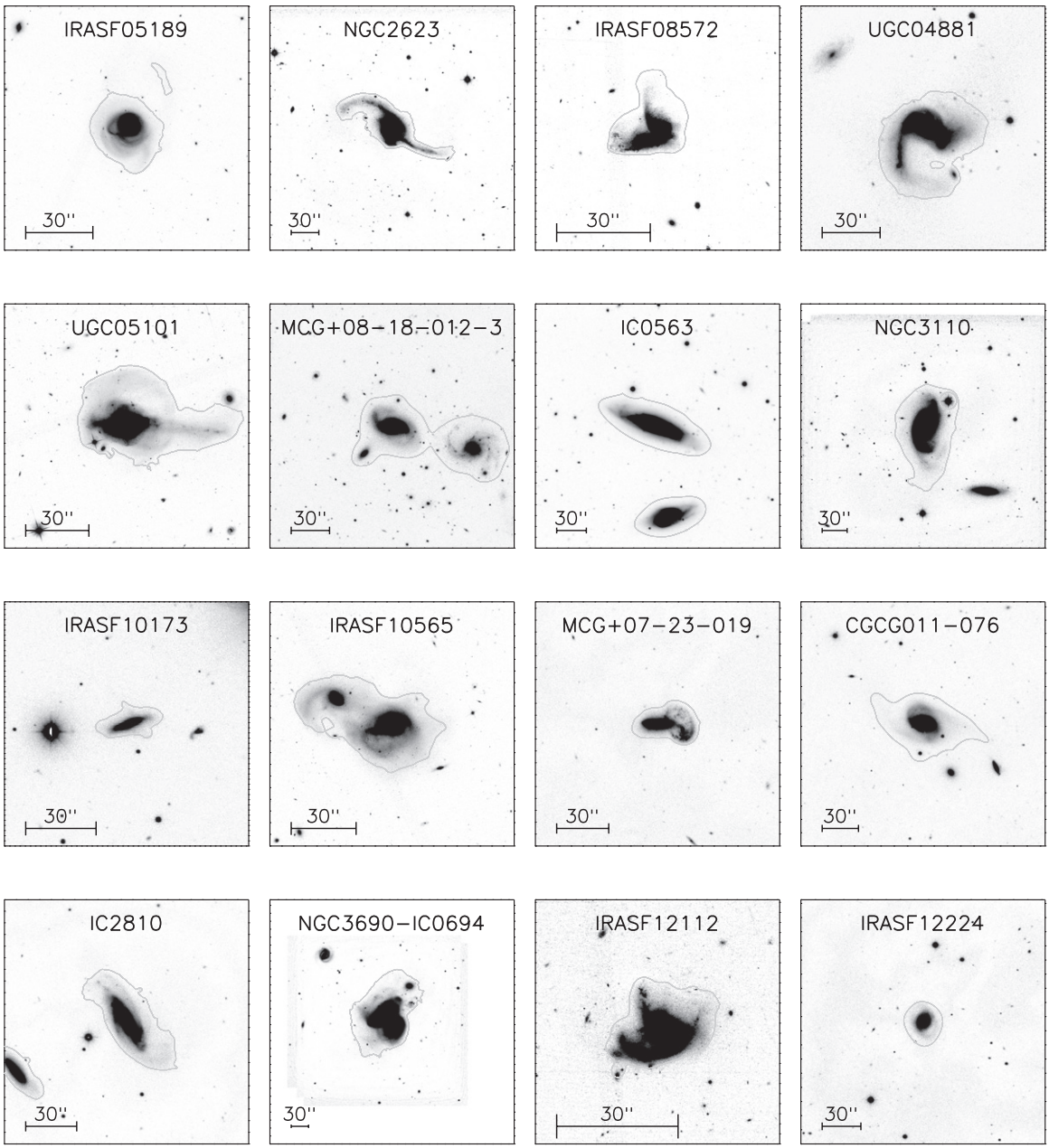

Figure 1. (Continued)

In Figure 6, we compare spectral indices: $\alpha_{0.23}^{0.54}$ versus $\alpha_{2.2}^{4.5}$ contrasts the slopes on either side of the stellar "bump;" $\alpha_{0.23}^{0.54}$ versus α_{8}^{24} contrasts the blueward slopes of the optical and the infrared "bumps," respectively; $\alpha_{2.2}^{4.5}$ versus α_{8}^{24} contrasts the redward and blueward slopes of the optical and infrared "bumps," respectively. The correlation coefficients for these three sets of comparisons are −0.08, −0.03, and −0.01. With this sample size, the conservative, non-directional *p*-values are 0.57, 0.83, and 0.94, respectively. This indicates that there is no correlation found between each pair of spectral indices. However, we note that for all three spectral index comparisons, the ULIRGs tend to show smaller values of α_{8}^{24} and $\alpha_{2.2}^{4.5}$, corresponding to a deeper trough at $\lambda \sim 4$–$8\,\mu$m, presumably due to greater silicate dust absorption of the continuum in ULIRGs. The physical significance of using $\alpha_{2.2}^{4.5}$ as an AGN indicator is further discussed in Section 5.1.5.

4.3. Flux Ratios

The SED shapes can also be characterized in terms of flux ratios with respect to the measured flux at 60 μm to compare direct stellar emission to dust emission. Figure 7 shows the distribution of flux ratios at radio (1.4 GHz), *J* band (1.2 μm), NUV (0.23 μm), and HX (2–10 keV), for all 11 ULIRGs and 53 LIRGs, where data are available. The wavelengths chosen for display represent the short and long wavelength extremes of the SEDs as well as the "peak" and the short wavelength side of the stellar thermal bump. For the *J*-band and NUV ratios, the difference in the distributions between ULIRGs and LIRGs is simply due to the well-known property of the SEDs where the thermal stellar "bump" remains relatively constant ($\lesssim$2) while the thermal dust "bump" grows by a factor of ∼10 (e.g., Sanders & Mirabel 1996). The different distributions for the LIRGs and ULIRGs point to the discrepant starlight-to-dust ratios in the

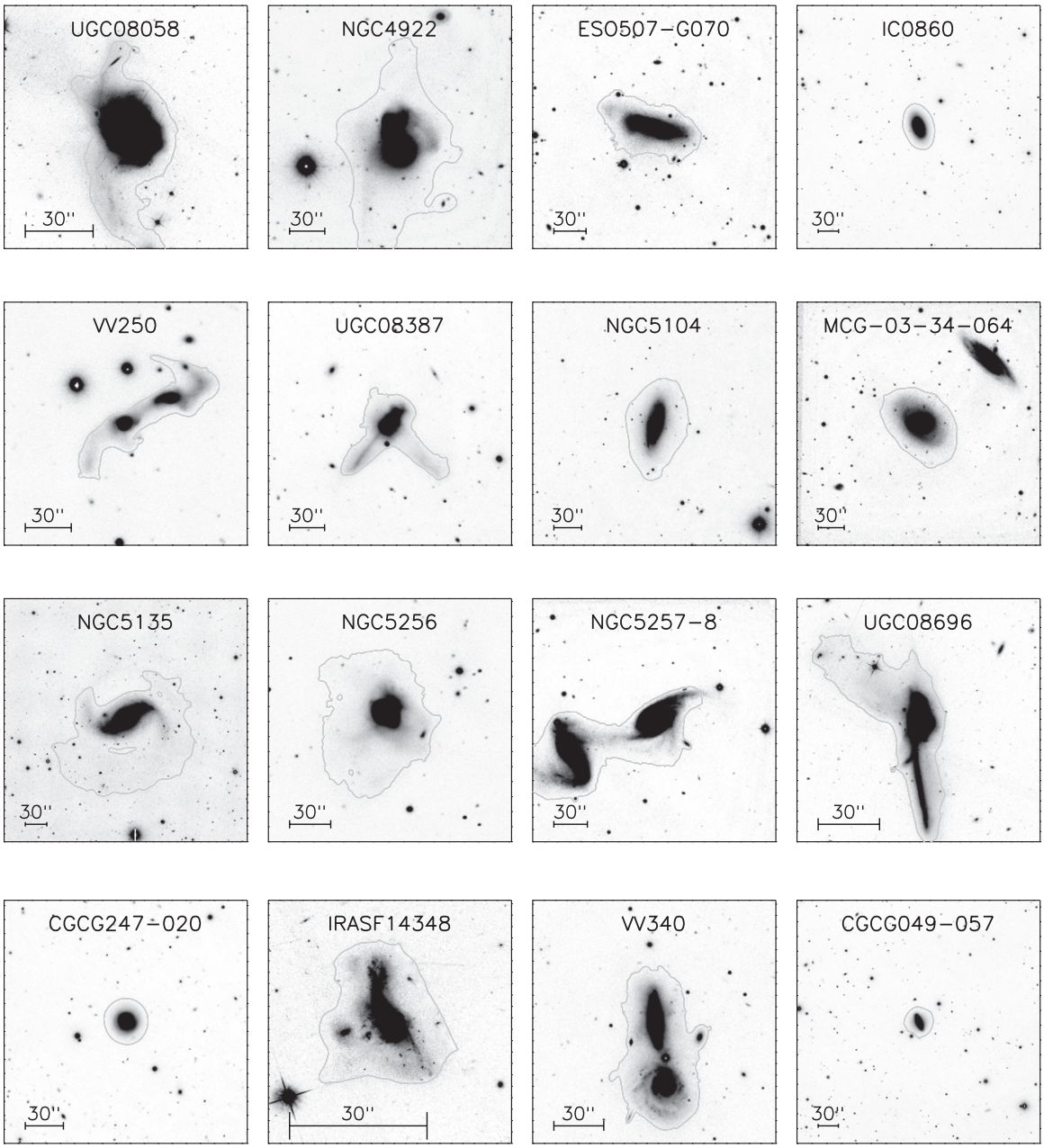

Figure 1. (Continued)

two populations. The HX band shows a somewhat surprising result in that the ratio seems to be similar for both LIRGs and ULIRGs.

Finally, we summarize the SEDs of our complete sample of (U)LIRGs in Table 8, which lists the relative mean luminosity, $R = \log[L_\nu(\text{band})/L_\nu(60\,\mu\text{m})]$, in all 26 observed bands with respect to the mean luminosity at 60 μm. Table 8 also lists the dispersion in the luminosity ratio, σ_R, and the full range, ΔR. The largest values of R are found at the long and short wavelength ends of the SEDs, where the emission is clearly not fit by the two (stellar and dust) thermal "bumps." However, it is interesting to note that a small dispersion in R is found in the radio (1.4 GHz), where the ratio is largest ($R = -5.81$). This would seem to confirm that the well-known "radio–infrared correlation" (e.g., Helou et al. 1985), also holds for (U)LIRGs.

At X-ray wavelengths, there seems to be a 0.4 dex increase in the mean luminosity in the HX band compared with the SX band. Of the 26 objects within our sample that are detected in both X-ray bands, ∼58% are more luminous in HX than in SX, suggesting the presence of an HX ionizing source. Due to the relative incompleteness of X-ray observations at the lower-luminosity end of our sample, this is slightly higher than the conservative estimate of 37% AGN fraction (or 48% if [Ne v] detection is taken into account) from an X-ray study of 44 GOALS (U)LIRGs at the high end of the $L_{\rm IR}$ range (with median $\log(L_{\rm IR}/L_\odot) = 11.99$; Iwasawa et al. 2011). Incorporating the entire GOALS sample, Petric et al. (2011) found that 18% of all (U)LIRGs contain an AGN based on a mid-IR *Spitzer*-IRS study; the comparatively lower fraction reflects that fewer of the lower-luminosity objects feature an AGN. We note that because of the complexity of dust geometry within these systems, discrepancies among the AGN fractions thus determined may be due to the limited sensitivity of the various AGN indicators.

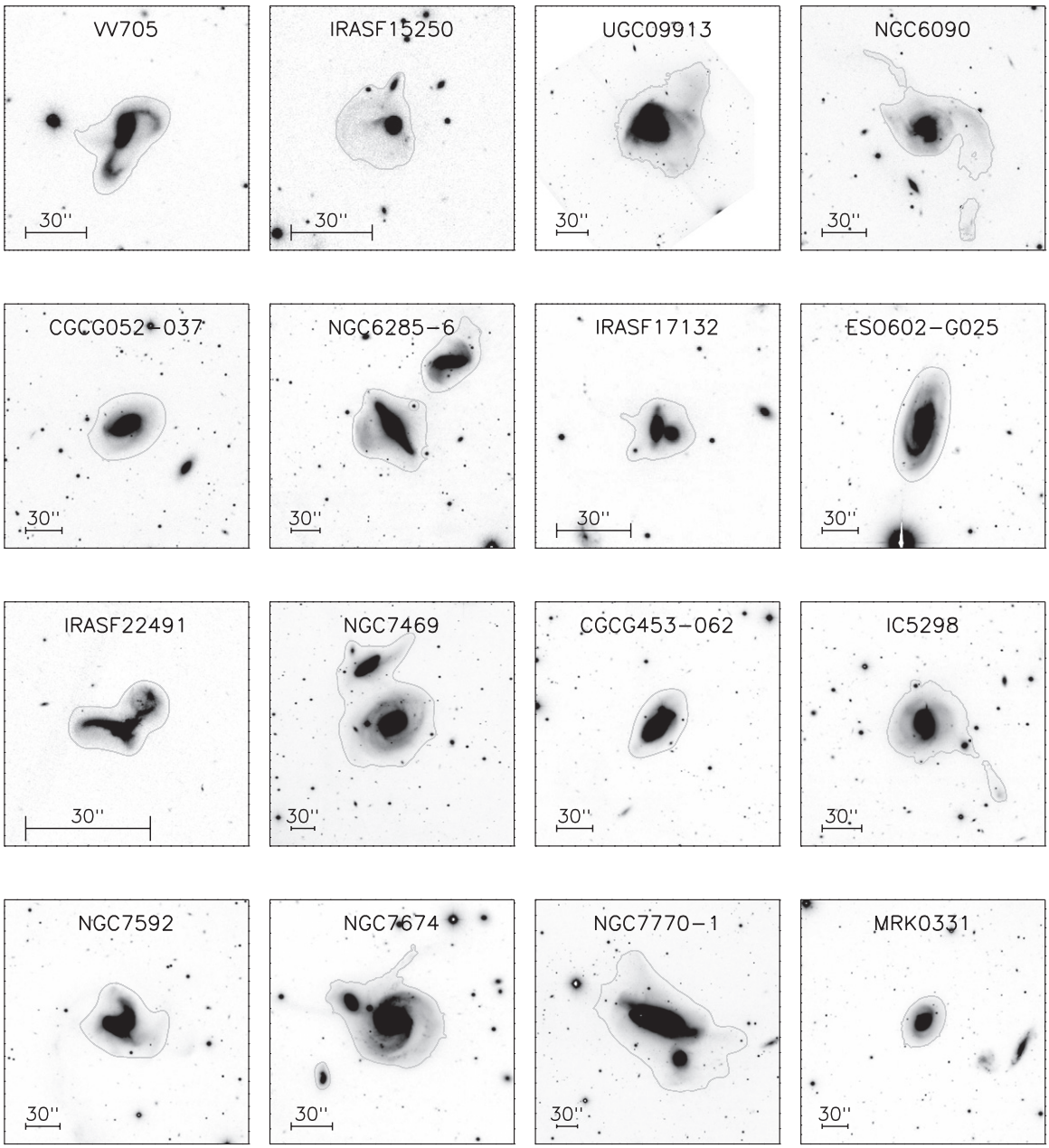

Figure 1. (Continued)

5. PHYSICAL PROPERTIES OF THE GOALS SAMPLE

Here we discuss the template fitting done to compute infrared luminosity and stellar mass; specifically, we fit the MIR–submillimeter portion of the SED with various dust models to compute L[8–1000 μm] and compare with previous estimates of $L_{\rm IR}$ computed from *IRAS* photometry. We use population synthesis models to fit the UV–NIR portion of the SED in order to determine stellar mass. These masses are then compared with stellar mass estimates computed using H-band luminosities alone.

5.1. Template Fits

We have fitted each of the (U)LIRG SEDs with stellar population synthesis and dust models (see Figure 2). Our goals are twofold: (1) to better determine stellar mass ($M_\star$) and subsequently star formation rate (SFR) of the local (U)LIRGs, and (2) to better estimate the flux at any unobserved wavelength band. The optical through NIR SED fitting has been done using the Le PHotometric Analysis for Redshift Estimations (Le PHARE[18]) code, a photometric redshift and simulation package developed by S. Arnouts and O. Ilbert. It is capable of providing optical and FIR fitting as well as a complete treatment of physical parameters and uncertainties based on the simple stellar population synthesis model of choice. As described below we consider both a Salpeter (Salpeter 1955) and Chabrier (Chabrier 2003) initial mass function (IMF) for all of our sources, plus a Calzetti extinction law (Calzetti et al. 1994) adopted throughout. Stellar masses were determined from fitting the observed data shortward of the K band.

[18] http://www.cfht.hawaii.edu/~arnouts/LEPHARE/cfht_lephare/lephare.html

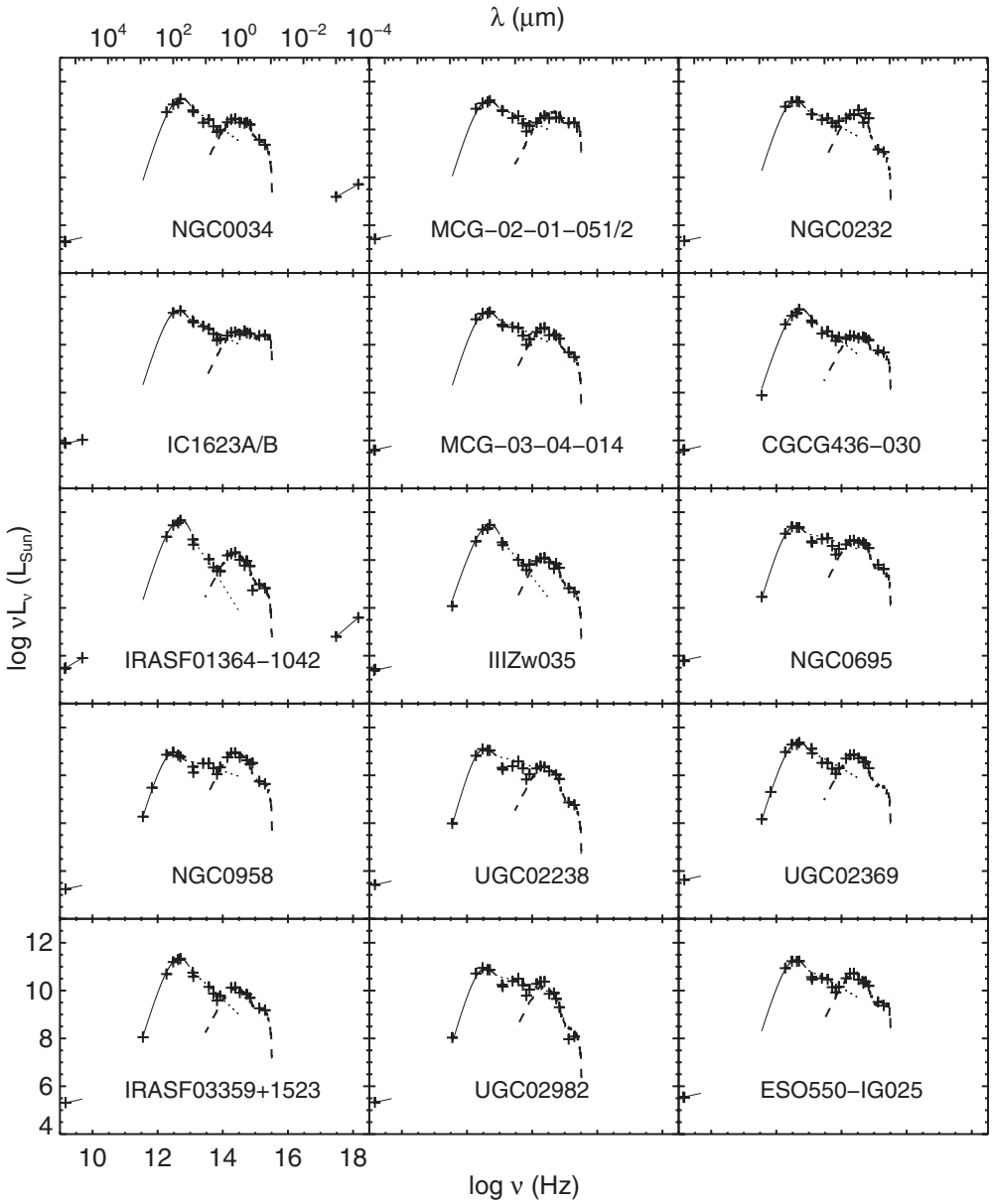

Figure 2. SEDs of the 64 objects in our sample in R.A. order. The units are log ν (Hz) on the x-axis and log νL_ν ($L_\odot$) on the y-axis. The crosses represent our photometry data points, while the dashed line illustrates the UV–NIR fit to Bruzual & Charlot (2003) stellar population synthesis models. The mBB graybody fit composes of the mid-infrared power-law portion (dotted) and the far-infrared blackbody portion (solid) in the SED.

5.1.1. Infrared Luminosities, Dust Temperatures, and Dust Masses

The infrared luminosity, $L_{\rm IR}$, that is discussed throughout this paper refers to the luminosity emitted in the wavelength range 8–1000 μm. The values of $L_{\rm IR}$ given in Table 1 have been adopted from the RBGS using the following prescription reproduced from Perault (1987) and Sanders & Mirabel (1996):

$$F_{\rm IR} = 1.8 \times 10^{-14}(13.45\,f_{12} + 5.16\,f_{25} + 2.58\,f_{60} + f_{100})\ [{\rm Wm}^{-2}], \quad (2)$$

$$L[8\text{–}1000\,\mu{\rm m}] = 4\pi\,D_L^2\,F_{\rm IR}\ [L_\odot], \quad (3)$$

where f_{12}, f_{25}, f_{60}, and f_{100} are the flux densities in Jy at 12, 25, 60, and 100 μm, respectively, and D_L is the luminosity distance.

Given the availability of our new IRAC, MIPS, and SCUBA data points, we can now test the above *IRAS* approximation and the validity of the assumed SED, in particular longward of 100 μm, for the local (U)LIRG population. We compute a new total infrared luminosity, $L_{\rm IR}$ = 8–1000 μm, by using χ^2 minimization to fit the MIR–FIR–submillimeter portion (14 data points) of the SEDs with different dust models and a modified blackbody fit (CE, DH, SK, mBB; Chary & Elbaz 2001; Dale & Helou 2002; Siebenmorgen & Krügel 2007; Casey 2012; Table 9). For the CE models, 105 templates with infrared luminosity ranging from $L_{\rm IR} = 10^{8.44}$ to $L_{\rm IR} = 10^{13.55}$ have been used. For the DH models, the 64 templates employed exhibit infrared luminosity within the range of $10^{8.32}$–$10^{14.34}$. The SK template library in LEPHARE consists of spatially integrated SEDs computed for starbursts of different radii, total luminosity, visual extinction, dust density within hot spots, and the luminosity ratio of hot spots to total as a secondary parameter based on Siebenmorgen & Krügel (2007). We utilized the models with radii = 1 kpc, $L_{\rm IR} = 10^{10.1}$–$10^{14.7}$, A_V = 2.2–119 mag, $n_{hs} = 10^2$–10^4 cm^{-3}, and OB luminosity to total

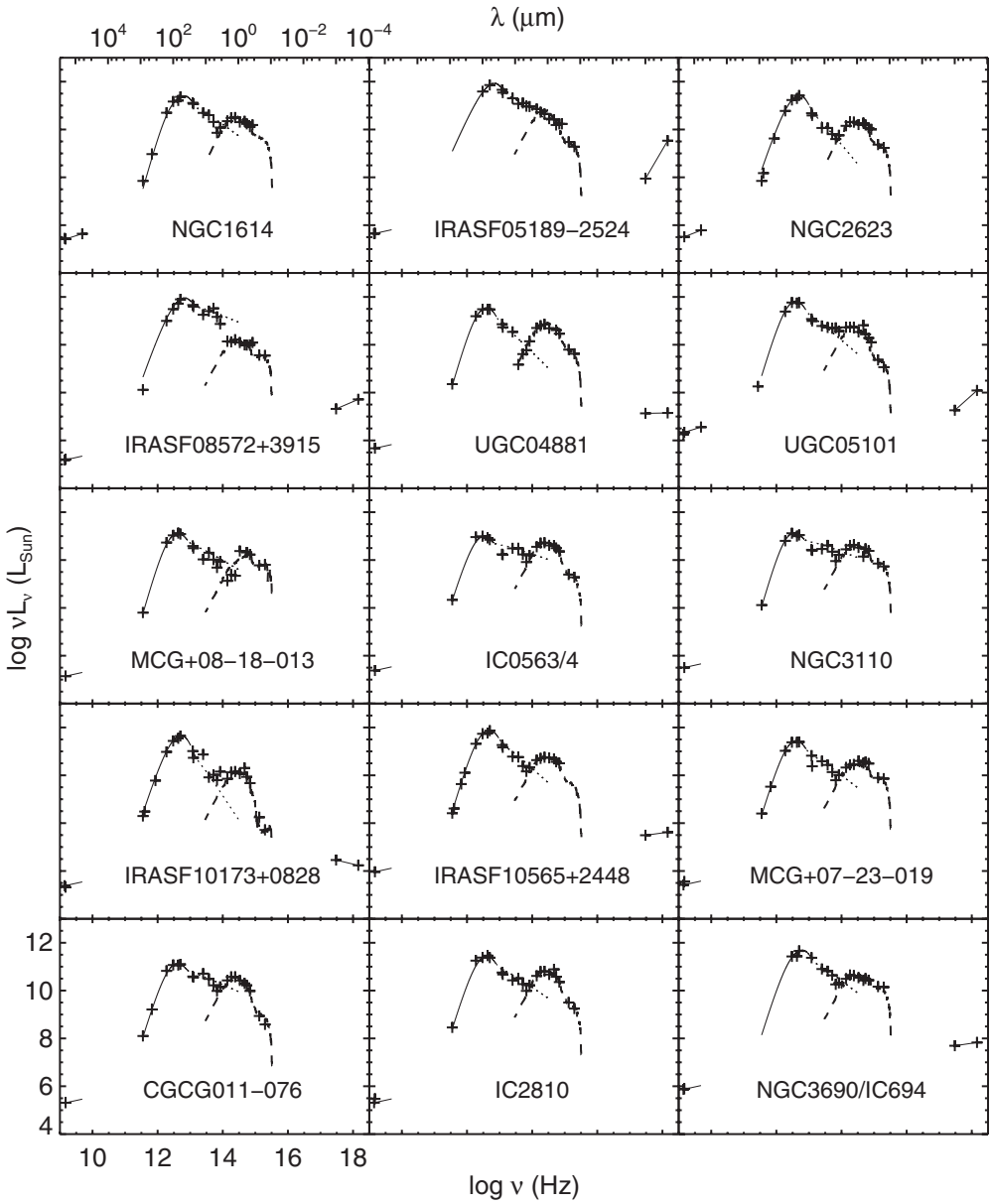

Figure 2. (Continued)

luminosity of 40%–90%. Lastly, the model-independent mBB fit is essentially the sum of a mid-infrared power law at $\lambda < 50\,\mu$m and a single-temperature graybody at $\lambda > 50\,\mu$m (Casey 2012):

$$S(\lambda) = N_{bb}\frac{\left(1 - e^{-\left(\frac{\lambda_0}{\lambda}\right)^{\beta}}\right)\left(\frac{c}{\lambda}\right)^3}{e^{hc/\lambda kT} - 1} + N_{pl}\lambda^{\alpha}e^{-\left(\frac{\lambda}{\lambda_c}\right)^2}, \quad (4)$$

where T is the far infrared dust temperature, λ_0 is the wavelength corresponding to an optical depth of unity, λ_c is the wavelength, where the mid-infrared power law turns over, β is the emissivity, and α is the spectral index of the power-law component. We let β and α vary to fit the SED where adequate data exist (see more details in Casey 2012).

The comparison of $L_{\rm IR}$ values is shown in Figure 8. The CE and DH model fits have large scatters (0.07 dex and 0.08 dex) around the *IRAS* values. The SK model fits exhibit a large scatter (0.05 dex) around the systematic offset of −0.03 dex from the *IRAS* luminosities. The mBB fit values are ∼0.02 dex systematically lower than the *IRAS* values, which translates to ∼5% of the infrared luminosity at $L_{\rm IR} = 10^{12}\,L_{\odot}$ level. The disagreement with the *IRAS* values is primarily due to the inadequate color assumptions implied in the coefficients of Equation (2). The scatter and discrepancy exhibited by the luminosities derived from the model-dependent templates are due to limitations in the step size within the model grids.

Comparing the fits of the different templates and the mBB at 12, 25, 60, 100, and 850 μm, the residuals between the data and the different fits are the smallest for mBB. The SK fits result in similarly minimal residuals except at the short wavelengths, whereas the CE and DH fit residuals exhibit the largest scatters. The main reason for the mismatch to the data is that the detailed infrared SED models have many degrees of freedom and very large template libraries at discrete temperatures and other grid parameters. In contrast, the analytical mBB fit provides more fitting flexibility and is designed to represent the data as

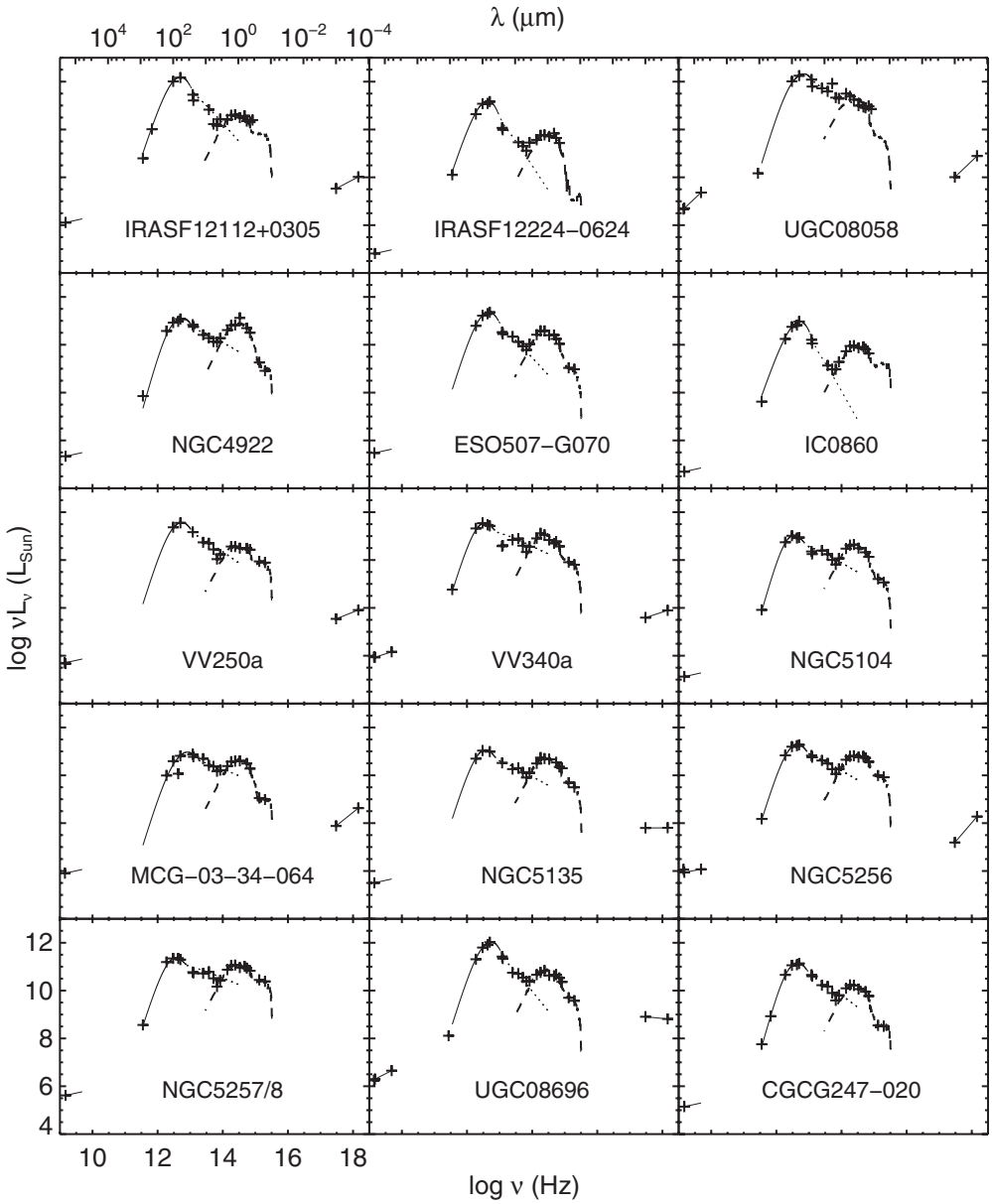

Figure 2. (Continued)

accurately as possible, despite having only three free parameters and not accounting for the mid-infrared polycyclic aromatic hydrocarbon features. Since for this paper we only measure $L_{\rm IR}$, $T_{\rm dust}$, and $M_{\rm dust}$, we choose to adopt the mBB fit results for the rest of the analyses.

Fitting graybody of a single dust temperature to the FIR SED from the blackbody peak ($\sim$100 μm) to 1000 μm, we determine and present the temperature of the dust in Table 9: mean $T_{\rm dust} = 33.2 \pm 6.2$ K. This temperature is $\sim$10 K cooler than that determined from the Perault (1987) prescription (see discussion in Casey 2012). With the lack of long-wavelength data points, the latter assumes a single-temperature dust emissivity model $\epsilon \propto \nu^{-1}$ fit to the fluxes in the four *IRAS* bands (as described in Sanders & Mirabel 1996), often adopting a peak shortward of the true peak now revealed when data points longward of 100 μm are present. The MIPS 160 μm and the SCUBA 850 μm points are invaluable for constraining the real peak, and this will be nailed when the *Herschel* far-infrared imaging observations are completed for the entire GOALS sample. Dust masses were calculated using the 850 μm flux from the SED and Equation (8) in Casey et al. (2011):

$$M_{\rm dust} = \frac{S_\nu D_{\rm L}^2}{\kappa_\nu B_\nu(T)} \propto \frac{D_{\rm L}^2}{\kappa_\nu \nu^2} \quad , \tag{5}$$

where S_ν is the flux density at frequency ν, κ_ν is the dust mass absorption coefficient at ν, $B_\nu(T)$ is the Planck function at temperature T, and $D_{\rm L}$ is the luminosity distance. We adopted a dust absorption coefficient of $\kappa_{850} = 0.15\ {\rm m^2\ kg^{-1}}$ (Weingartner & Draine 2001; Dunne et al. 2003). We derived a mean dust temperature $M_{\rm dust} = 10^{7.3}\ M_\odot$ for the sample.

We note that dust temperatures and masses depend critically on a thorough understanding of the radiative transfer involved as well as the underlying geometry of the dust cloud. This dust temperature can be taken as a characteristic $T_{\rm dust}$ for the system (measured from the peak of the SED). Clearly the physics of these galaxies is more complex, comprised of many dust reservoirs of different temperatures. Unfortunately, investigating this is beyond the current scope of observations and

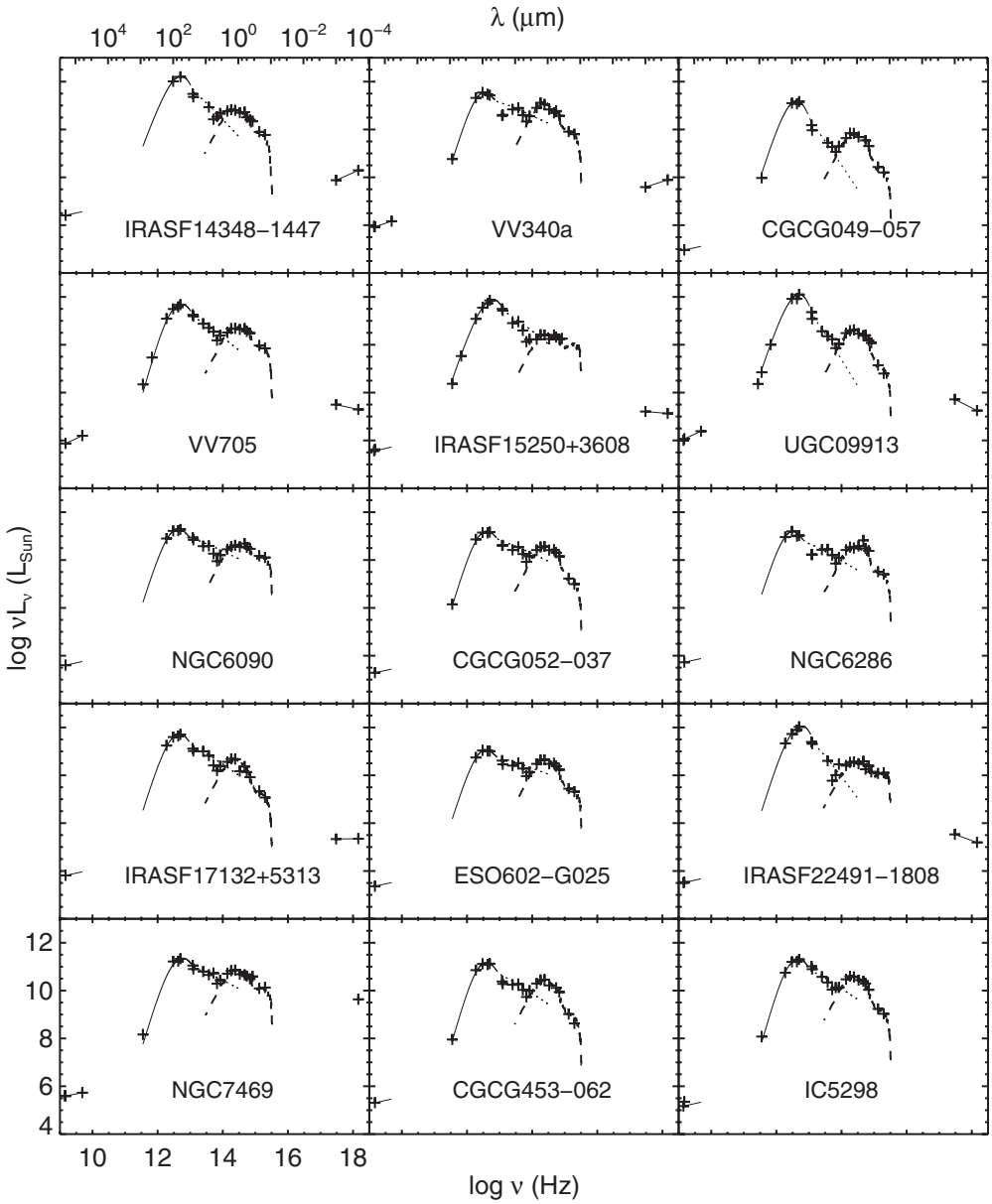

Figure 2. (Continued)

this work. We included our derivation of the dust temperature primarily as a baseline for comparison to the high-z universe, though we caution that the physical interpretation of that quantity remains uncertain.

5.1.2. Stellar Masses

Stellar masses for the (U)LIRGs in our sample have been computed via two methods using two different IMFs, and the resulting masses are given in Table 10. Here, we discuss the differences among these measurements.

The two methods adopted for mass determination were to fit the UV–NIR part of the SEDs and to scale from the H-band luminosity. The H band is usually selected for stellar mass conversion because it is at or near the photospheric peak of the stellar SED, and is thought not to be contaminated by hot dust emission from AGNs (Hainline et al. 2011). However, problems with H-band scaling may also arise due to thermally pulsing asymptotic giant branch stars for SEDs with a significant contribution from young stellar populations (Walcher et al. 2011). On the other hand, the SED-fitted masses encompass the stellar component contributing to the optical peak, taking into account the treatment of dust with the designated dust extinction law. For the ensuing discussion, we focus on comparing the SED-fitted masses derived from using two different IMFs.

Our optical–NIR SED fitting procedure is based on stellar population synthesis models from Bruzual & Charlot (2003) using 10 different broadband UV, optical, and infrared bands. Two different IMFs were used: a Chabrier IMF (Chabrier 2003) and a Salpeter IMF (Salpeter 1955). Since the IMF dictates the scaling of the mass-to-light (M/L) ratio in converting luminosity to mass via its slope and mass cutoffs, we compare the masses derived from these two IMFs and assess their differences (Figure 9). The lower and upper mass cutoffs employed were 0.1 $M_{\odot}$ and 100 $M_{\odot}$, respectively (Bruzual & Charlot 2003); no additional adjustments to the parameters of the IMFs have been made. The models assumed a star formation history with SFH $= e^{-t/\tau}$, where τ, varying

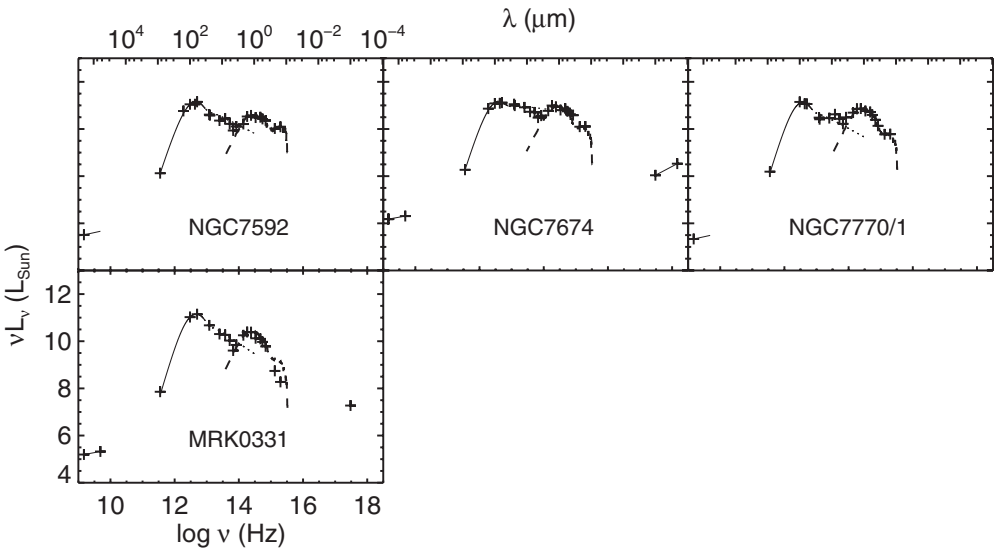

Figure 2. (Continued)

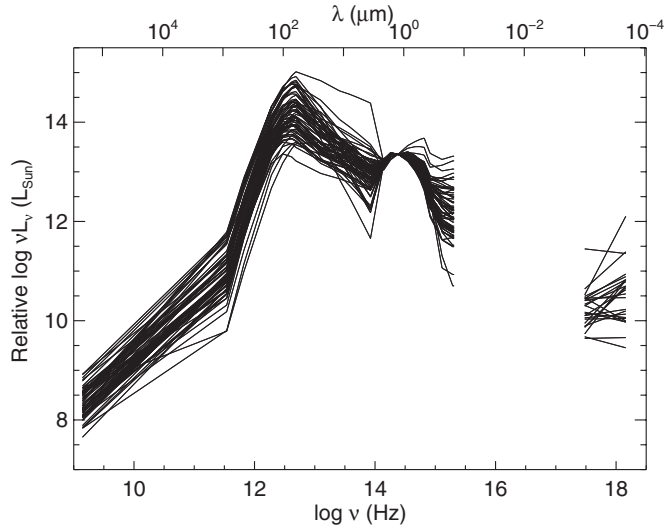

Figure 3. Full radio through X-ray SEDs normalized at *J* band (near the peak of the stellar portion) for all 64 (U)LIRGs. The discrete data points represent photometry fitted at the 27 observed bands. Lines connecting the data points have been drawn to help guide the eye except for the regime between the far-UV and soft X-ray bands.

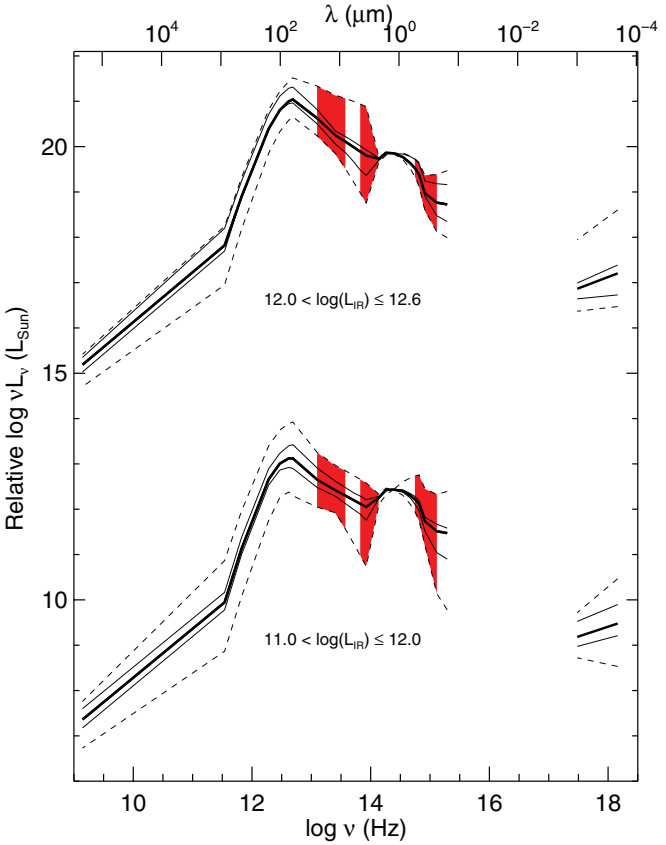

Figure 4. Mean radio through X-ray SEDs normalized at *J* band in two luminosity bins corresponding to ULIRGs (top) and LIRGs (bottom). The 50% and 100% range for the SEDs are shown by the thin solid and dashed lines, respectively. The shaded regions mark the wavelength ranges used to calculate the three spectral indices, α_2^1, as described in the text.

from 1–30, is the *e*-folding parameter in years. The metallicity ($Z = 0.004$, 0.008, and0.02) has been treated as a free parameter as well.

In general, the mean difference between the masses derived from both methods is at the level of 0.26 ± 0.41 dex, with the masses generally being underestimated from the Salpeter IMF. This was unexpected given that Salpeter IMF tends to result in higher stellar masses due to the difference in treatment of the low-mass end—the Chabrier IMF tends to be flatter and therefore more physical. Under the same input parameters the stellar models with Chabrier IMF fitted the UV light in our SEDs better than their Salpeter counterparts. We also note that the Chabrier IMF incorporates a more up-to-date treatment of UV radiation from young stars in starburst populations, and thus the Chabrier masses have been adopted as the stellar masses for the local (U)LIRGs.

5.1.3. Comparison of $M_\star$ and L_{IR}

Figure 10 shows the (U)LIRGs as a distribution of SED-fitted mass in logarithmic scale. All but 3 of the 64 objects fall within 2σ of the mean mass, $\log(M_\star/M_\odot) = 10.79 \pm 0.40$.

For the individual subsamples of 53 LIRGs and 11 ULIRGs, we find the mean stellar masses to be $\log(M_\star/M_\odot) = 10.75 \pm$

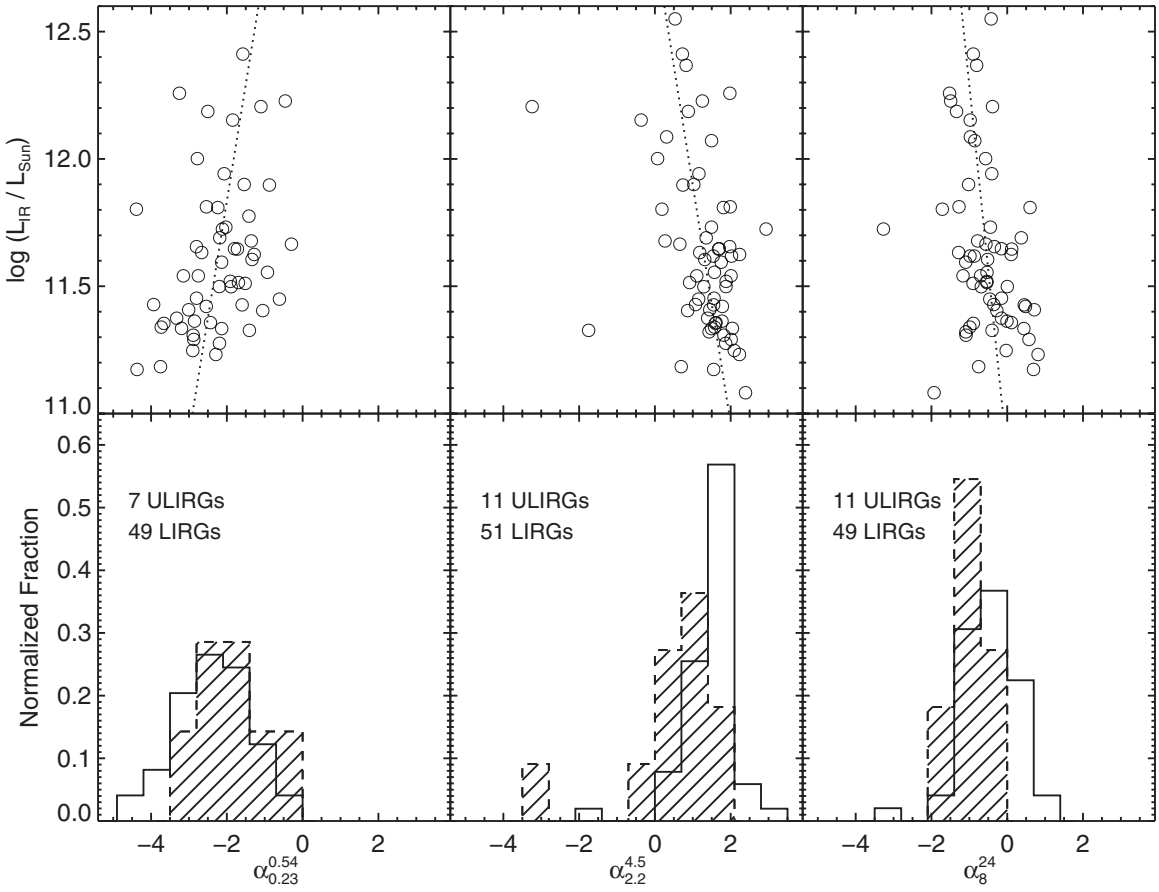

Figure 5. Spectral indices ($\alpha_{0.23}^{0.54}$, $\alpha_{2.2}^{4.5}$, and α_{8}^{24}) plotted against infrared luminosity (top), and their corresponding histograms (bottom). The best-fit (dotted) line within each of the top three panels shows the trends of the indices with increasing luminosity. The numbers of (U)LIRGs that are used to compute these indices (due to availability in the corresponding photometry data) are listed in the upper left-hand corner of the histograms. The hashed histograms represent ULIRGs, while the open histograms represent LIRGs.

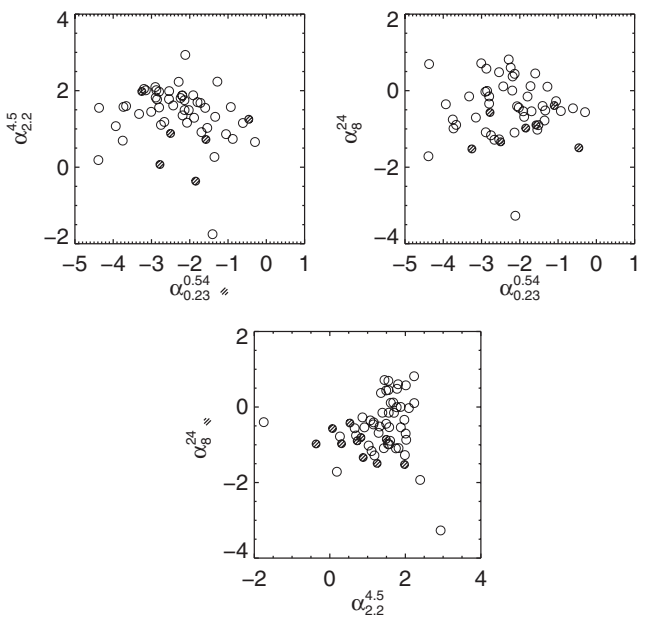

Figure 6. Comparison of spectral indices ($\alpha_{0.23}^{0.54}$, $\alpha_{2.2}^{4.5}$, and α_{8}^{24}) for ULIRGs (hashed circles) and LIRGs (open circles). In the panels with the mid-IR index α_{8}^{24}, the ULIRGs tend to cluster in a small region on the plot due to their very dusty nature, but the near-IR index $\alpha_{2.2}^{4.5}$ does not work as well in distinguishing the ULIRGs from their lower-luminosity counterparts.

0.39 for the LIRGs, and $\log(M_\star/M_\odot) = 11.00 \pm 0.40$ for the ULIRGs. The factor of ∼2 lower mean stellar mass for LIRGs is primarily due to a decreasing "low-mass tail" of objects with masses in the range $\log(M_\star/M_\odot) = 9.3$–$10.3$. On the other extreme, the most massive object (UGC 08058 = Mrk 231) appears to show hot dust emission from the central AGN, which contributes about 20% of the *H*-band flux (Surace & Sanders 1999, 2000). Thus for this one object, we have corrected the fitted stellar mass accordingly.

Our results are consistent with estimates of the mass of objects of similar luminosity at higher redshift: $\log(M_{\rm ULIRG}/M_\odot) \sim 10.51 \pm 0.45$ (from Takagi et al. 2003, where the two-tailed unpaired *p*-value for the differences between our ULIRG masses gives 0.052, which is not statistically significant); and $\log(M_{\rm LIRG}/M_\odot) \sim 10.5$ (from Melbourne et al. 2008, who found that (U)LIRGs are more massive than "normal," non-LIRG galaxies that are morphologically irregular and spiral galaxies from the GOODS-S field, where $\log(M_{\rm normal}/M_\odot) \sim 9.5$).

5.1.4. Star Formation Rates

Using the light contribution from the UV and IR, we determine the SFR for the unobscured and obscured stellar populations, respectively. The recipe from Wuyts et al. (2011) gives the following calibration for converting from infrared and

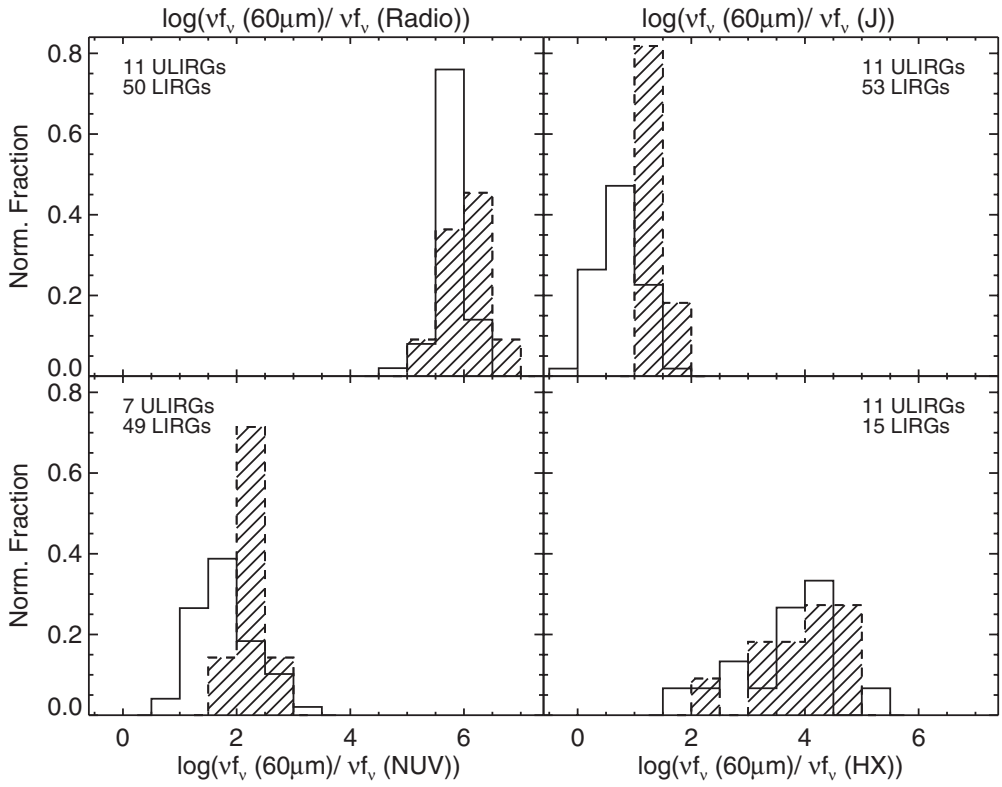

Figure 7. Normalized histograms of logarithmic ratios for νf_ν at 60 μm to that at radio (1.4 GHz), J band (1.2 μm), NUV (0.23 μm), and HX (2–10 keV). These histograms are normalized by the number of LIRGs (open histograms) and ULIRGs (hatched histograms) in each plot (as listed in the upper corners), as restricted by the availability of the photometry data used in these ratios.

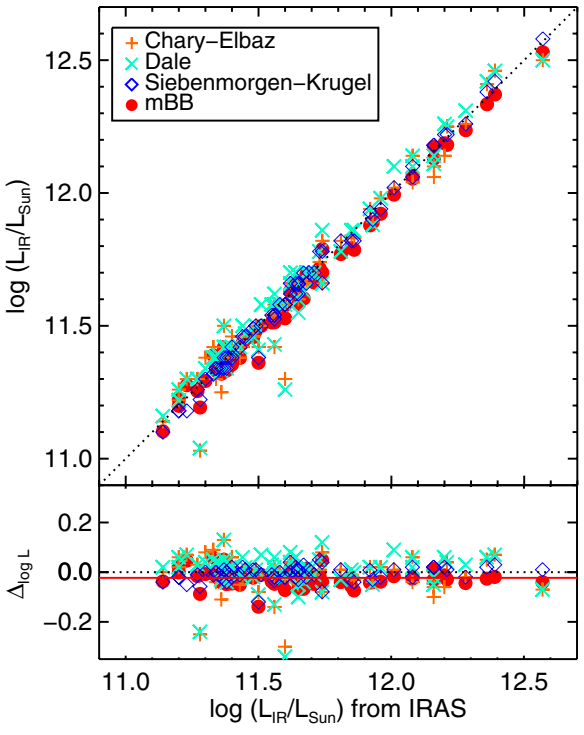

Figure 8. Comparison of the $L_{\rm IR}$ derived from *IRAS* fluxes and from fitting the FIR-submillimeter part of the SEDs for the (U)LIRGs (CE: orange cross, DH: cyan X, SK: blue open diamonds, and mBB: red filled circles). The dotted lines indicate linear correlation with zero offsets. As a one-to-one correspondence is expected, the residual $\Delta_{\log L} \equiv \log(L_{\rm fit}/L_\odot) - \log(L_{IRAS}/L_\odot)$ shows the scatter around the values predicted from *IRAS*. The red dash-dotted line shows that the mean of the mBB values is offset by 0.021 dex.

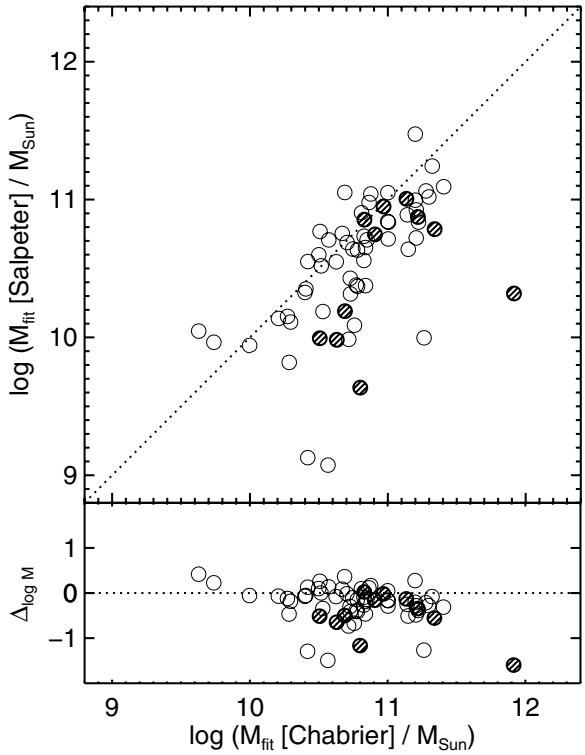

Figure 9. Comparison of the stellar mass estimates derived from fitting the UV–NIR part of the Salpeter-based BC03 SEDs and from that of the Chabrier-based ones. The residual plot illustrates that $\Delta_{\log M} \equiv \log(M_{\rm Sal}/M_\odot) - \log(M_{\rm Chab}/M_\odot)$ centers at -0.26, with the 25th percentile at -0.41 and the 75th percentile at -0.02. The open circles are LIRGs and hatched circles are ULIRGs. The dotted lines indicate linear correlation with zero offset.

Table 6
Mean SED Templates

log ν (Hz)	λ (μm)	Band (Name)	log νL_ν ($L_\odot$) (ULIRGs)	log νL_ν ($L_\odot$) (LIRGs)
18.16	2.07E-04	HX	8.20	7.68
17.48	9.93E-04	SX	7.86	7.39
15.29	0.15	FUV	9.72	9.68
15.11	0.23	NUV	9.76	9.72
14.91	0.37	*U*	9.97	9.94
14.82	0.46	*B*	10.38	10.32
14.75	0.54	*V*	10.52	10.42
14.67	0.65	*R*	10.64	10.51
14.54	0.86	*I*	10.77	10.61
14.38	1.24	*J*	10.85	10.64
14.26	1.65	*H*	10.86	10.63
14.14	2.17	*K*	10.73	10.47
13.93	3.56	IRAC1	10.80	10.25
13.82	4.51	IRAC2	10.89	10.33
13.72	5.76	IRAC3	10.98	10.40
13.58	7.96	IRAC4	11.11	10.50
13.41	11.60	IRAS1	11.24	10.62
13.10	23.84	MIPS1	11.62	10.86
13.10	23.88	IRAS2	11.62	10.86
12.69	61.49	IRAS3	12.04	11.33
12.62	72.56	MIPS2	11.99	11.32
12.47	101.98	IRAS4	11.80	11.21
12.28	156.96	MIPS3	11.39	10.86
11.82	449.57	SCUBA1	9.89	9.33
11.54	866.77	SCUBA2	8.82	8.15
9.15	2.14E05	VLA	6.19	5.57

Table 7
Spectral Index versus L_{IR}

λ range (μm)	α_j^i (index)	$\bar{\alpha}$ (LIRGs)	$\bar{\alpha}$ (ULIRGs)	r
0.23–0.54	$\alpha_{0.23}^{0.54}$	-2.29 ± 0.94	-1.80 ± 0.78	+0.32
2.2–4.5	$\alpha_{2.2}^{4.5}$	$+1.49 \pm 0.70$	$+0.84 \pm 0.69$	−0.30
8.0–24.0	α_{8}^{24}	-0.47 ± 0.76	-0.93 ± 0.39	−0.38

monochromatic UV luminosity at 2800 Å to SFR:

$$\mathrm{SFR_{UV+IR}}[M_\odot\,\mathrm{yr}^{-1}] = 1.09 \times 10^{-10}(L_{\mathrm{IR}} + 3.3L_{2800})/L_\odot \quad . \tag{6}$$

Decomposing this quantity into separate UV and IR components, we consider the contribution to the total SFR from the UV and IR luminosities individually (Table 11). $\mathrm{SFR_{UV}}$ ranges from <1 to ∼10 $M_\odot\,\mathrm{yr}^{-1}$, while $\mathrm{SFR_{IR}}$ is up to ∼50 times larger. We show the fold enrichment of $\mathrm{SFR_{IR}}$ to $\mathrm{SFR_{UV}}$ as a function of infrared luminosity in Figure 11. The logarithmic difference for the LIRGs centered at 1.49 ± 0.66 dex, while that for the ULIRGs is more clustered at 1.90 ± 0.24 dex. This figure highlights that while the infrared SFR in ULIRGs is ∼100 times that determined from the UV, the fold enrichment in the LIRGs is only ∼30 times with a large scatter potentially due to the large variations in dust geometry (i.e., single spirals undergoing minor merger events as opposed to major-merging pairs).

The mean log $\mathrm{SFR_{UV+IR}}$ for the GOALS ULIRGs is 2.25 ± 0.16 and that for the LIRGs is 1.57 ± 0.19. Corresponding specific SFRs (sSFR = $\mathrm{SFR_{UV+IR}}/M_\star$) have been computed and are also listed in Table 11. The effect on SFR from UV emission and trends with infrared luminosity as seen in the GOALS (U)LIRGs as well as the comparison to a nearby lower-luminosity sample (SINGS; Kennicutt et al. 2003) have been discussed extensively in Howell et al. (2010). Compared with the Howell et al. (2010) sample (with median sSFR = $3.9 \times 10^{-10}\,\mathrm{yr}^{-1}$), the median sSFR of our sample is $6.8 \times 10^{-10}\,\mathrm{yr}^{-1}$, or equivalent to a mass-doubling timescale of 1.5 Gyr. Our median sSFR value is higher because the *GALEX* sample is more complete at the lower-luminosity end (with less extinction by dust). The slope of the log sSFR–log$M_\star$ relation is −0.78 (or 0.22 in log SFR–log$M_\star$ space) for the (U)LIRGs, which is shallower than that reported for the high-z infrared main-sequence galaxies (Rodighiero et al. 2011; Daddi et al. 2007).

Table 8
Variations in SEDs of (U)LIRGs

log ν (Hz)	λ (μm)	Band (Name)	R	σ_R	ΔR
18.16	2.07E-04	HX	−3.10	0.81	3.73
17.48	9.93E-04	SX	−3.69	0.54	2.24
15.23	0.15	FUV	−1.88	0.61	3.18
15.11	0.23	NUV	−1.83	0.56	2.88
14.91	0.37	*U*	−1.62	0.48	1.70
14.82	0.46	*B*	−1.23	0.47	1.68
14.75	0.54	*V*	−1.12	0.45	1.72
14.67	0.65	*R*	−1.03	0.44	1.76
14.54	0.86	*I*	−0.92	0.44	1.82
14.38	1.24	*J*	−0.88	0.43	1.82
14.26	1.65	*H*	−0.88	0.44	1.82
14.14	2.17	*K*	−1.04	0.43	1.80
13.93	3.56	IRAC1	−1.15	0.50	2.45
13.82	4.51	IRAC2	−1.07	0.46	2.22
13.72	5.76	IRAC3	−0.99	0.42	1.98
13.58	7.96	IRAC4	−0.88	0.36	1.68
13.41	11.60	IRAS1	−0.75	0.30	1.34
13.10	23.84	MIPS1	−0.44	0.17	0.95
13.10	23.88	IRAS2	−0.44	0.17	0.95
12.69	61.49	IRAS3	0.00	0.00	0.00
12.62	72.56	MIPS2	−0.02	0.05	0.19
12.47	101.98	IRAS4	−0.17	0.13	0.53
12.28	156.96	MIPS3	−0.55	0.19	0.84
11.82	449.57	SCUBA1	−2.07	0.25	1.16
11.54	866.77	SCUBA2	−3.20	0.29	1.34
9.15	2.14E05	VLA	−5.81	0.28	1.75

Notes. SEDs normalized at 60 μm for the complete sample of 53 LIRGs and 11 ULIRGS. Band names correspond to the filters used in Tables 4 and 5. R corresponds to the ratio log $[(\nu L_\nu(\lambda))/(\nu L_\nu(60\,\mu\mathrm{m}))]$.

5.1.5. AGN Indicators

Different wavelengths offer different methods for diagnosing AGN candidates; a multi-wavelength SED study allows simultaneous access to these various indicators and may be used to evaluate their effectiveness. We employ the radio–infrared flux ratio (q) as defined by Condon et al. (1991) and the criteria specified by Yun et al. (2001; radio-excess: $q < 1.64$; infrared-excess: $q > 3.0$) as the basis of our comparison. Figure 12 shows q plotted as a function of L_{IR} along with its distribution in the right panels. The mean $\langle q \rangle = 2.41 \pm 0.29$ for the sample. With these limits, there are two LIRGs (with $L_{\mathrm{IR}} < 11.6$) identified as radio-excess sources. These objects may be potential AGN hosts with a compact radio core or radio jets and lobes (Kartaltepe et al. 2010; Sanders & Mirabel 1996).

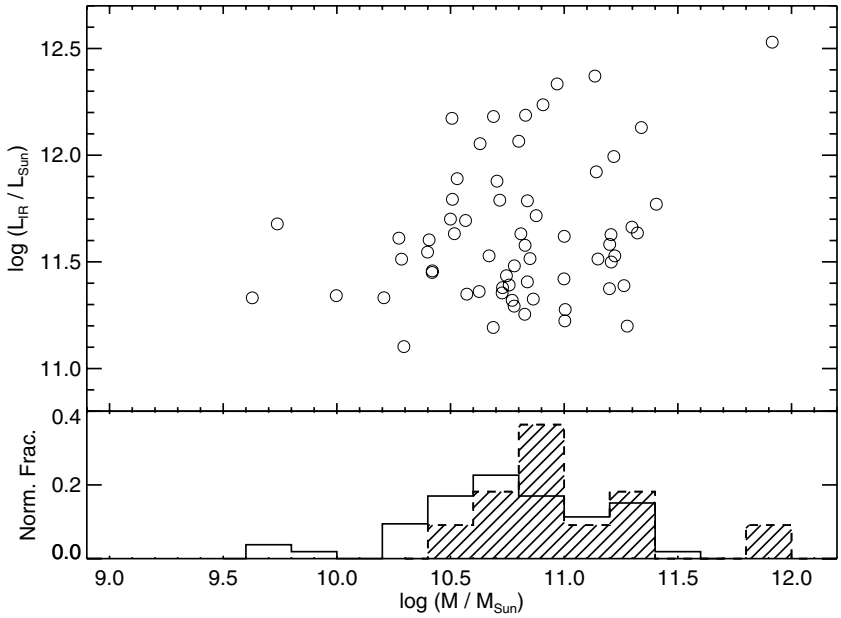

Figure 10. mBB infrared luminosity vs. stellar mass as derived from template fitting in logarithmic scale for our sample. The range of the masses spans more than a factor of 10 for the LIRGs. This is more clearly visualized in the histogram at the bottom, with bin width of 0.15 dex. The open histogram with solid line represents the LIRGs, while the hatched histogram represents the ULIRGs.

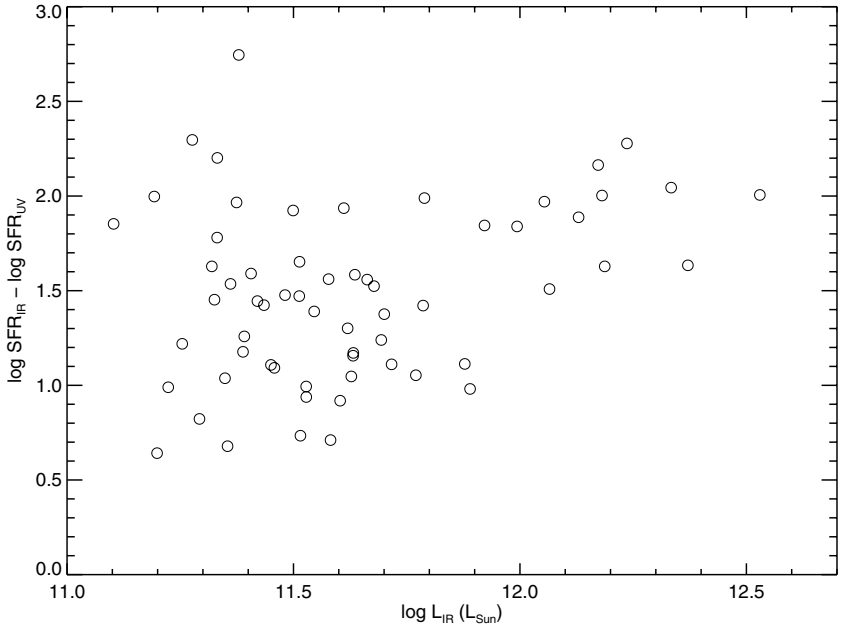

Figure 11. Logarithmic difference in SFR determined from the IR and the UV vs. $L_{\rm IR}$. The positive values in this difference reflect that the UV-derived SFR underpredict the SFR as measured from IR light.

On the other end, both of the infrared-excess sources are ULIRGs, which may be hosting dense and compact starbursts, or a dust-enshrouded AGN.

For objects with X-ray detection, we define two different criteria for identifying X-ray AGNs: (1) $L_{\rm HX} > 10^{42}\,{\rm erg\,s^{-1}}$ (Kartaltepe et al. 2010) and (2) hardness ratio, HR > -0.3 (Iwasawa et al. 2011). Seven systems qualified as an X-ray AGN by the first criterion, six by the second, and three of these objects were identified by both. Both radio-excess sources are very luminous in the HX band. All the HR > -0.3 AGN candidates are ULIRGs, though there may be a selection bias since all 11 of 11 ULIRGs in the GOALS sample have been observed and detected in the X-ray, but only 16 of 53 LIRGs have been observed thus far. *Chandra* observations of the lower-luminosity LIRGs have been proposed and awarded in Cycle 14 (PI: Sanders) to complete the sample.

Power-law SED provides a complementary way to select AGNs that might be heavily obscured and opaque to HX emission. We apply a criterion based on $\log(\nu L_{4.5}) - \log(\nu L_{2.2}) > 0$ to select galaxies with power-law SED shape in the near-IR, corresponding to F_ν spectral slope of 0.4 (Kartaltepe et al. 2010; Alonso-Herrero et al. 2006; Donley et al. 2007).

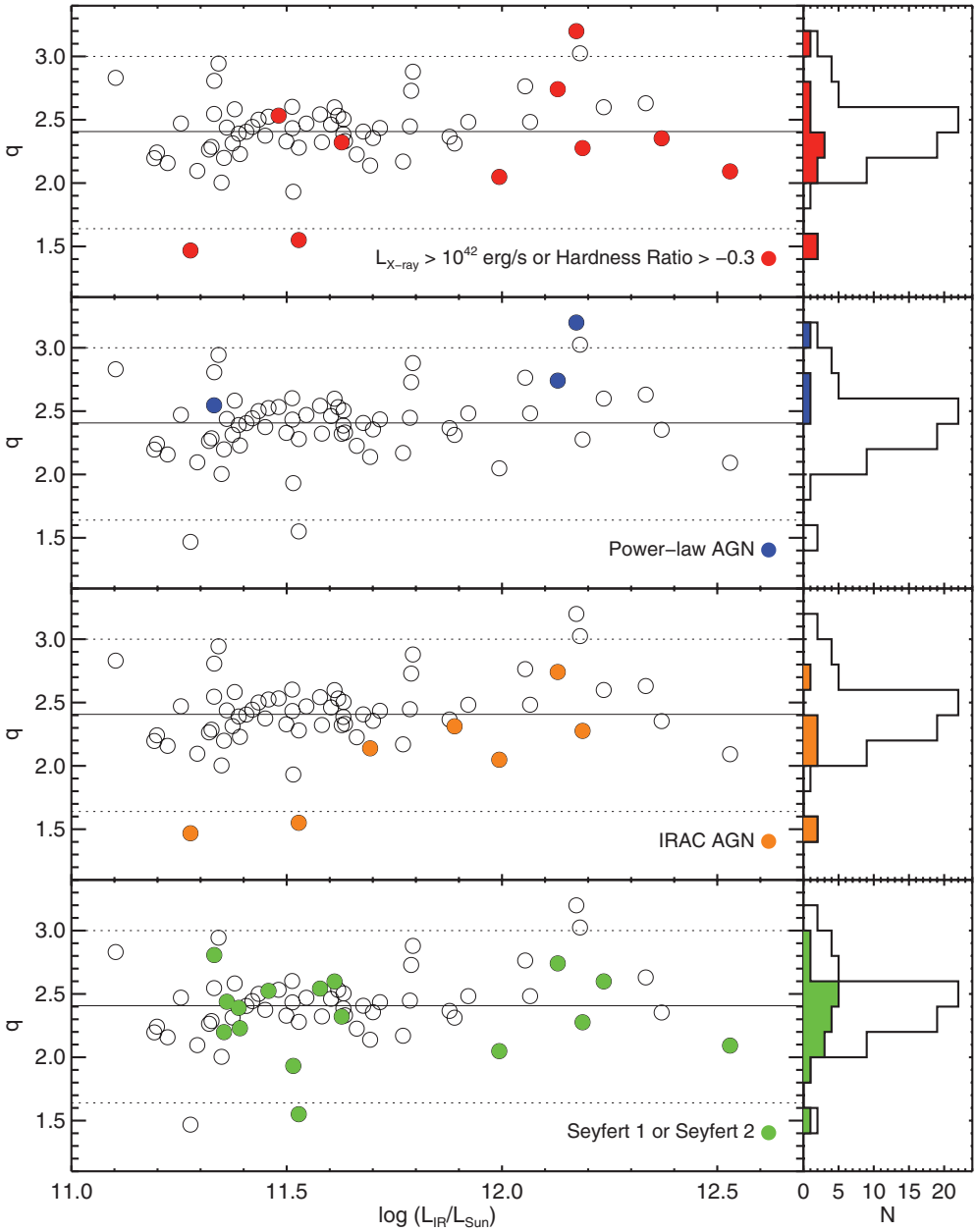

Figure 12. q vs. νL_{IR} plots shown for the 64 (U)LIRGs along with the distribution in q on the right panels. The solid line indicates the median value ($q = 2.41$) of the sample, with $\sigma = 0.29$. The dotted lines indicate the radio-excess ($q < 1.64$) and infrared-excess ($q > 3.0$) criteria from Yun et al. (2001). From top to bottom are four different AGN indicators (filled circles/histograms): X-ray luminosity and hardness ratio, power-law slope, IRAC colors, and optical spectral classification.

Only three power-law AGN candidates are identified in the sample, and the two ULIRGs among these are both X-ray AGN candidates.

Additional MIR-based selection criteria have been devised to identify heavily obscured AGNs missed in deep X-ray surveys. In particular, selection based on IRAC color cuts (Lacy et al. 2004; Stern et al. 2005) is insensitive to obscuration but can trace AGN-heated dust, providing a powerful technique for discerning luminous obscured and unobscured AGNs. The revised IRAC color selection by Donley et al. (2012) is designed to incorporate the best aspects of the current IRAC wedges but to minimize star-forming contaminants and has been adopted here for selecting IRAC AGN candidates (see Equations (1) and (2) in Donley et al. 2012). This set of criteria results in seven IRAC AGN candidates in our sample, two of them being ULIRGs. Interestingly, most of the IRAC AGNs are below the median q of the sample ($q_{med} = 2.41$), with two of them being radio-excess sources.

Our last AGN indicator comparison involves selection based on optical emission line diagnostics. Yuan et al. (2010) applied a Sloan Digital Sky Survey based semiempirical optical spectral classification scheme to a large sample of local infrared galaxies, 57 of which are in our current sample. Among these, two are Seyfert 1 galaxies and 14 are Seyfert 2 systems. These Seyferts bear a distribution in q similar to that of the entire sample.

Table 9
Derived Infrared Luminosities, Dust Temperatures, and Dust Masses

RBGS Name	$\log (L_{IR})_{mBB}$ ($L_\odot$)	T_{dust} (K)	$\log (M_{dust})$ ($M_\odot$)
NGC 0034	11.48 ± 0.01	37.64 ± 0.40	6.88 ± 0.06
MCG-02-01-051/2	11.46 ± 0.02	32.70 ± 0.57	7.11 ± 0.06
NGC 0232	11.43 ± 0.01	28.35 ± 0.18	7.41 ± 0.06
IC1623A/B	11.66 ± 0.01	31.45 ± 0.15	7.42 ± 0.06
MCG-03-04-014	11.63 ± 0.02	31.09 ± 0.50	7.42 ± 0.06
CGCG436-030	11.68 ± 0.02	39.05 ± 0.80	7.14 ± 0.06
IRASF01364-1042	11.79 ± 0.02	35.37 ± 0.65	7.36 ± 0.06
IIIZw035	11.62 ± 0.02	35.86 ± 0.65	7.35 ± 0.06
NGC 0695	11.69 ± 0.02	27.90 ± 0.36	7.54 ± 0.06
NGC 0958	11.22 ± 0.02	23.42 ± 0.32	7.55 ± 0.06
UGC02238	11.39 ± 0.01	26.34 ± 0.24	7.13 ± 0.06
UGC02369	11.60 ± 0.02	34.01 ± 0.52	7.18 ± 0.06
IRASF03359+1523	11.51 ± 0.03	33.62 ± 0.78	7.12 ± 0.06
UGC02982	11.20 ± 0.02	27.33 ± 0.45	6.96 ± 0.06
ESO550-IG025	11.50 ± 0.02	28.95 ± 0.36	7.44 ± 0.06
NGC 1614	11.61 ± 0.01	42.23 ± 0.15	6.45 ± 0.06
IRASF05189-2524	12.13 ± 0.01	46.20 ± 0.22	8.02 ± 0.06
NGC 2623	11.58 ± 0.02	35.78 ± 0.42	7.35 ± 0.06
IRASF08572+3915	12.17 ± 0.04	46.09 ± 1.12	7.60 ± 0.06
UGC04881	11.70 ± 0.02	28.62 ± 0.42	7.43 ± 0.06
UGC05101	12.00 ± 0.01	28.75 ± 0.28	7.83 ± 0.06
MCG+08-18-013	11.33 ± 0.02	29.83 ± 0.58	6.86 ± 0.06
IC0563/4	11.28 ± 0.01	24.30 ± 0.21	7.57 ± 0.06
NGC 3110	11.41 ± 0.01	25.98 ± 0.16	7.26 ± 0.06
IRASF10173+0828	11.79 ± 0.02	36.78 ± 0.72	7.43 ± 0.06
IRASF10565+2448	12.05 ± 0.02	33.62 ± 0.50	7.54 ± 0.06
MCG+07-23-019	11.63 ± 0.02	29.35 ± 0.42	7.47 ± 0.06
CGCG011-076	11.38 ± 0.03	29.62 ± 0.77	7.18 ± 0.06
IC2810	11.64 ± 0.02	28.95 ± 0.43	7.56 ± 0.06
NGC 3690/IC694	11.89 ± 0.01	41.36 ± 0.05	7.09 ± 0.06
IRASF12112+0305	12.33 ± 0.03	35.78 ± 0.75	8.06 ± 0.06
IRASF12224-0624	11.32 ± 0.03	31.23 ± 0.64	7.32 ± 0.06
UGC08058	12.53 ± 0.01	45.67 ± 0.13	7.50 ± 0.06
NGC 4922	11.33 ± 0.02	37.81 ± 0.67	6.32 ± 0.06
ESO507-G070	11.53 ± 0.01	33.31 ± 0.42	7.19 ± 0.06
IC0860	11.10 ± 0.02	37.29 ± 0.41	6.84 ± 0.06
VV250a	11.77 ± 0.01	37.81 ± 0.31	7.15 ± 0.06
UGC08387	11.72 ± 0.01	30.31 ± 0.28	7.28 ± 0.06
NGC 5104	11.25 ± 0.01	26.10 ± 0.29	7.03 ± 0.06
MCG-03-34-064	11.19 ± 0.01	53.90 ± 0.64	5.89 ± 0.06
NGC 5135	11.29 ± 0.01	27.26 ± 0.15	7.35 ± 0.06
NGC 5256	11.52 ± 0.02	31.45 ± 0.59	7.22 ± 0.06
NGC 5257/8	11.63 ± 0.01	27.14 ± 0.23	7.70 ± 0.06
UGC08696	12.18 ± 0.01	37.81 ± 0.15	7.57 ± 0.06
CGCG247-020	11.35 ± 0.02	31.16 ± 0.66	6.72 ± 0.06
IRASF14348-1447	12.37 ± 0.35	37.03 ± 5.09	8.35 ± 0.09
VV340a	11.79 ± 0.02	25.80 ± 0.28	7.92 ± 0.06
CGCG049-057	11.33 ± 0.01	30.59 ± 0.32	7.23 ± 0.06
VV705	11.88 ± 0.01	37.03 ± 0.38	7.00 ± 0.06
IRASF15250+3608	12.07 ± 0.02	43.61 ± 0.64	7.49 ± 0.06
UGC09913	12.24 ± 0.01	35.69 ± 0.10	8.00 ± 0.06
NGC 6090	11.55 ± 0.02	30.95 ± 0.37	7.34 ± 0.06
CGCG052-037	11.45 ± 0.02	29.15 ± 0.41	7.22 ± 0.06
NGC 6286	11.42 ± 0.01	23.86 ± 0.11	7.81 ± 0.06
IRASF17132+5313	11.92 ± 0.02	33.01 ± 0.53	7.61 ± 0.06
ESO602-G025	11.34 ± 0.01	27.77 ± 0.31	7.37 ± 0.06
IRASF22491-1808	12.19 ± 0.02	40.79 ± 0.88	7.49 ± 0.06
NGC 7469	11.58 ± 0.01	39.96 ± 0.32	6.74 ± 0.06
CGCG453-062	11.37 ± 0.02	28.55 ± 0.45	7.01 ± 0.06
IC5298	11.53 ± 0.01	32.63 ± 0.46	6.88 ± 0.06
NGC 7592	11.39 ± 0.02	32.33 ± 0.59	7.21 ± 0.06
NGC 7674	11.51 ± 0.03	28.42 ± 0.51	7.44 ± 0.06
NGC 7771	11.35 ± 0.03	27.20 ± 0.48	7.28 ± 0.06
MRK0331	11.36 ± 0.01	32.70 ± 0.41	6.74 ± 0.06

Table 10
Derived Stellar Masses

RBGS Name	$\log (M_{fit})_{Sal}$ ($M_\odot$)	$\log (M_H)_{Sal}$ ($M_\odot$)	$\log (M_{fit})_{Cha}$ ($M_\odot$)	$\log (M_H)_{Cha}$ ($M_\odot$)
(1)	(2)	(3)	(4)	(5)
NGC 0034	10.44	10.58	10.41	10.07
MCG-02-01-051/2	9.15	10.65	10.42	10.15
NGC 0232	10.72	10.84	11.05	10.34
IC1623A/B	9.07	10.65	10.56	10.15
MCG-03-04-014	10.89	10.85	10.79	10.35
CGCG436-030	9.97	10.56	9.74	10.06
IRASF01364-1042	10.65	10.45	10.75	9.95
IIIZw035	10.15	10.25	10.26	9.75
NGC 0695	11.04	11.03	11.29	10.53
NGC 0958	11.05	11.14	11.27	10.63
UGC02238	10.36	10.55	10.74	10.04
UGC02369	11.19	11.03	11.29	10.53
IRASF03359+1523	10.73	10.29	11.09	9.79
UGC02982	11.07	10.54	10.76	10.04
ESO550-IG025	10.94	10.93	11.22	10.43
NGC 1614	10.51	10.63	10.51	10.13
IRASF05189-2524	10.97	10.91	11.36	10.41
NGC 2623	10.31	10.47	10.38	9.96
IRASF08572+3915	10.12	10.29	10.51	9.81
UGC04881	11.04	10.97	10.86	10.47
UGC05101	10.86	10.93	11.23	10.43
MCG+08-18-013	9.86	9.56	9.27	9.06
IC0563/4	10.72	10.87	10.95	10.36
NGC 3110	10.45	10.83	10.72	10.32
IRASF10173+0828	10.81	10.33	10.55	9.84
IRASF10565+2448	9.59	10.87	10.76	10.38
MCG+07-23-019	10.37	10.63	10.37	10.14
CGCG011-076	10.65	10.75	10.84	10.25
IC2810	11.05	10.99	11.01	10.49
NGC 3690/IC694	10.17	10.76	10.52	10.26
IRASF12112+0305	10.92	10.76	11.05	10.28
IRASF12224-0624	9.95	9.95	9.99	9.45
UGC08058	10.32	11.48	11.92	10.98
NGC 4922	11.48	10.97	11.19	10.47
ESO507-G070	10.64	10.78	11.15	10.28
IC0860	10.12	10.12	10.29	9.62
VV250a	10.24	10.39	10.31	10.02
UGC08387	10.55	10.59	10.45	10.08
NGC 5104	10.56	10.81	10.83	10.29
MCG-03-34-064	10.84	10.75	11.01	10.25
NGC 5135	10.65	10.97	10.82	10.46
NGC 5256	10.72	11.01	10.85	10.51
NGC 5257/8	11.01	11.23	11.21	10.73
UGC08696	10.86	10.96	10.84	10.46
CGCG247-020	10.36	10.45	10.76	9.95
IRASF14348-1447	10.76	11.02	11.07	10.54
VV340a	10.82	10.83	11.07	10.31
CGCG049-057	10.15	10.02	10.21	9.52
VV705	10.68	10.86	10.71	10.37
IRASF15250+3608	9.91	10.61	10.57	10.11
UGC09913	10.71	10.81	10.88	10.29
NGC 6090	10.75	10.73	10.66	10.23
CGCG052-037	10.65	10.72	10.75	10.25
NGC 6286	10.73	10.76	10.62	10.26
IRASF17132+5313	11.43	10.89	11.25	10.39
ESO602-G025	10.96	10.82	10.84	10.31
IRASF22491-1808	10.37	10.71	10.77	10.23
NGC 7469	11.02	11.05	10.85	10.54
CGCG453-062	10.55	10.62	10.63	10.12
IC5298	10.73	10.76	10.83	10.26
NGC 7592	10.07	10.73	10.75	10.23
NGC 7674	10.85	11.17	11.23	10.67
NGC 7770/1	10.02	11.08	11.28	10.57
MRK0331	10.21	9.67	10.19	9.88

Notes. Column 2: Mass fit (UV–opt SED) with Salpeter IMF (Salpeter 1955). Column 3: Mass fit (H band) with Salpeter IMF (Salpeter 1955). Column 4: Mass fit (UV–opt SED) with Chabrier IMF (Chabrier 2003). Column 5: Mass fit (H band) with Chabrier IMF (Chabrier 2003).

Table 11
SFR and sSFR for Local (U)LIRGs

RBGS Name	log SFR_{UV} ($M_\odot$ yr^{-1})	log SFR_{IR} ($M_\odot$ yr^{-1})	log SFR_{UV+IR} ($M_\odot$ yr^{-1})	log $sSFR_{UV+IR}$ (yr^{-1})
NGC 0034	0.40	1.50	1.54	−8.88
MCG-02-01-051/2	0.38	1.50	1.53	−8.89
NGC 0232	0.01	1.47	1.49	−9.51
IC1623A/B	0.49	1.72	1.74	−8.82
MCG-03-04-014	0.51	1.68	1.71	−9.10
CGCG436-030	0.19	1.71	1.72	−8.02
IRASF01364-1042	−0.16	1.80	1.81	−8.91
IIIZw035	−0.29	1.65	1.66	−8.61
NGC 0695	0.14	1.69	1.71	−9.59
NGC 0958	0.59	1.21	1.31	−9.97
UGC02238	−0.27	1.34	1.35	−9.42
UGC02369	0.09	1.69	1.70	−9.63
IRASF03359+1523	0.08	1.56	1.57	−8.71
UGC02982	−0.77	1.21	1.21	−9.48
ESO550-IG025	−0.39	1.54	1.54	−9.67
NGC 1614	0.50	1.68	1.71	−8.81
IRASF05189-2524	0.28	2.19	2.19	−9.14
NGC 2623	0.19	1.60	1.62	−8.78
IRASF08572+3915	0.05	2.21	2.21	−8.29
UGC04881	0.64	1.74	1.77	−9.10
UGC05101	0.19	2.02	2.03	−9.19
MCG+08-18-013	−0.41	1.35	1.36	−8.27
IC0563/4	0.27	1.23	1.28	−9.72
NGC 3110	0.71	1.38	1.47	−9.26
IRASF10173+0828	−2.27	1.87	1.87	−8.64
IRASF10565+2448	0.59	2.11	2.12	−8.68
MCG+07-23-019	0.72	1.64	1.69	−8.71
CGCG011-076	−0.15	1.46	1.47	−9.37
IC2810	0.36	1.66	1.68	−9.32
NGC 3690/IC694	0.95	1.95	1.99	−8.54
IRASF12112+0305	0.33	2.35	2.36	−8.61
IRASF12224-0624	−2.44	1.37	1.37	−8.63
UGC08058	0.56	2.58	2.58	−9.33
NGC 4922	−0.55	1.39	1.40	−9.80
ESO507-G070	−0.10	1.56	1.57	−9.58
IC0860	−0.71	1.11	1.12	−9.18
VV250a	0.40	1.79	1.81	−9.03
UGC08387	0.36	1.73	1.75	−8.75
NGC 5104	0.07	1.25	1.28	−9.55
MCG-03-34-064	−0.98	1.32	1.32	−9.68
NGC 5135	0.51	1.33	1.39	−9.39
NGC 5256	0.82	1.59	1.65	−9.20
NGC 5257/8	0.91	1.63	1.71	−9.49
UGC08696	0.60	2.21	2.22	−8.61
CGCG247-020	−1.33	1.39	1.40	−9.33
IRASF14348-1447	0.77	2.39	2.40	−8.73
VV340a	0.75	1.77	1.81	−9.60
CGCG049-057	−0.83	1.36	1.36	−8.85
VV705	0.80	1.92	1.95	−8.75
IRASF15250+3608	0.12	2.09	2.09	−8.54
UGC09913	−0.01	2.26	2.27	−8.64
NGC 6090	0.63	1.59	1.63	−9.04
CGCG052-037	0.05	1.47	1.49	−9.26
NGC 6286	0.35	1.38	1.42	−9.15
IRASF17132+5313	0.11	1.97	1.98	−9.16
ESO602-G025	−0.09	1.35	1.36	−9.50
IRASF22491-1808	0.22	2.21	2.22	−8.47
NGC 7469	0.62	1.68	1.71	−9.49
CGCG453-062	−0.14	1.39	1.40	−9.22
IC5298	0.05	1.62	1.63	−9.20
NGC 7592	0.17	1.40	1.42	−9.33
NGC 7674	0.57	1.59	1.63	−9.60
NGC 7771	0.25	1.40	1.43	−9.83
MRK0331	0.04	1.52	1.54	−9.24

6. CONCLUSIONS

We have used common aperture masks for the first time to assemble accurate radio through X-ray SEDs of a complete local sample of 53 LIRGs and 11 ULIRGs observable from the northern hemisphere ($\delta > -30^\circ$ and $|b| > 30^\circ$). We have utilized several new large data sets provided by GOALS's space- and ground-based observations of (U)LIRGs along with additional archival data from the literature and our own previously unpublished ground-based optical–NIR data from Mauna Kea in our analysis of these SEDs. We summarize our findings as follows.

1. The SEDs for all objects are similar in that they show a broad, thermal stellar peak (∼0.3–2 μm), and a dominant FIR (∼40–200 μm) thermal dust peak, where $\nu f_\nu(60\,\mu\mathrm{m})/\nu f_\nu(V)$ varies from ∼2 to 30 with increasing L_{IR}. The logarithmic difference between the stellar and dust peaks is 1.2 dex for the ULIRGs and 0.7 dex for the LIRGs.
2. When normalized at *IRAS* 60 μm, the largest range in the luminosity ratio, $R(\lambda) \equiv \log[\nu L_\nu(\lambda)/\nu L_\nu(60\,\mu\mathrm{m})]$, observed over the full sample is seen in the hard X-rays (HX = 2–10 keV), where $\Delta R_{HX} = 3.73$ ($\bar{R}_{HX} = -3.10$). A small range is found in the radio (1.4 GHz), $\Delta R_{1.4\,GHz} = 1.75$, where the mean ratio is largest, ($\bar{R}_{1.4\,GHz} = -5.81$).
3. Infrared luminosities, $L_{IR}(8\text{–}1000)\,\mu$m), have been recomputed using a modified blackbody fit (Casey et al. 2011) to the MIR–FIR–submillimeter SEDs. The new L_{IR} values are overall ∼0.02 dex lower than the original *IRAS* values (Sanders et al. 2003), primarily due to the disagreement with the color indices implied in the coefficients of the Perault (1987) equation. The simple, analytical blackbody fit results have thus been adopted in determining the FIR properties of the (U)LIRGs (e.g., L_{IR}, T_{dust}, and M_{dust}).
4. The stellar masses computed using BC03 for LIRGs, $\log(M_{LIRGs}/M_\odot) = 10.75 \pm 0.39$, and ULIRGs, $\log(M_{ULIRGs}/M_\odot) = 11.00 \pm 0.40$, are consistent with mass estimates of higher redshift LIRGs from Melbourne et al. (2008) and with mass estimates of higher redshift ULIRGs from Takagi et al. (2003), respectively.
5. SFRs determined from infrared and monochromatic UV luminosities individually have been compared: SFR_{UV} ranges from <1 to ∼10 $M_\odot$ yr^{-1}, while SFR_{IR} is up to ∼50 times larger. The logarithmic difference for the ULIRGs is much more clustered (1.90 ± 0.24 dex) than for the LIRGs (1.49 ± 0.66 dex), plausibly due to large variations in dust geometry among the lower-luminosity objects.
6. Radio–infrared flux ratio (q), along with other multi-wavelength criteria, has been assessed as different AGN indicators. The results among the various selection techniques complement each other. About 60% of the ULIRGs (and 25% of the LIRGs) would be classified as an AGN by at least one of the selection criteria.

V.U. thanks O. Ilbert and S. Arnouts for their help with using the Le PHARE code, C. J. Ma for his help with UH 2.2 m data acquisition and reduction, T.-T. Yuan for her help with various scientific and technical contributions, and C. W. K. Chiang for statistical consult and technical help with Figures 1 and 3. V.U. also extends appreciation toward the UH TAC for their generous support of this project in awarding telescope time on Mauna Kea, as well as Colin Aspin and the UH 2.2 m Telescope staff

for their help and support in the acquisition of the ground-based optical photometry. This research has made use of the NASA/IPAC Extragalactic Database (NED) and IPAC Infrared Science Archive, which are operated by the Jet Propulsion Laboratory, California Institute of Technology, under contract with the National Aeronautics and Space Administration. This publication has also made use of data products from the Two Micron All Sky Survey, which is a joint project of the University of Massachusetts and the Infrared Processing and Analysis Center/California Institute of Technology, funded by the National Aeronautics and Space Administration and the National Science Foundation. V.U. wishes to acknowledge funding support from the NASA Harriet G. Jenkins Predoctoral Fellowship Project and Giovanni Fazio via the Smithsonian Astrophysical Observatory Predoctoral Fellowship and JPL Contract/IRAC GTO Grant 1256790. This paper is dedicated to the memory of Michele Dufault, who led the effort to obtain accurate large aperature photometric optical and near-infrared data for our complete sample of objects, and whose early work was critical in our decision to publish this paper.

REFERENCES

Alonso-Herrero, A., Pérez-González, P. G., Alexander, D. M., et al. 2006, ApJ, 640, 167
Armus, L., Mazzarella, J. M., Evans, A. S., et al. 2009, PASP, 121, 559
Bruzual, G., & Charlot, S. 2003, MNRAS, 344, 1000
Calzetti, D., Kinney, A. L., & Storchi-Bergmann, T. 1994, ApJ, 429, 582
Casey, C. M. 2012, MNRAS, 425, 3094
Casey, C. M., Chapman, S. C., Neri, R., et al. 2011, MNRAS, 415, 2723
Chabrier, G. 2003, PASP, 115, 763
Chary, R., & Elbaz, D. 2001, ApJ, 556, 562
Condon, J. J., Helou, G., Sanders, D. B., & Soifer, B. T. 1990, ApJS, 73, 359
Condon, J. J., Helou, G., Sanders, D. B., & Soifer, B. T. 1996, ApJS, 103, 81
Condon, J. J., Huang, Z., Yin, Q. F., & Thuan, T. X. 1991, ApJ, 378, 65
Daddi, E., Dickinson, M., Morrison, G., et al. 2007, ApJ, 670, 156
Dale, D. A., & Helou, G. 2002, ApJ, 576, 159
Donley, J. L., Koekemoer, A. M., Brusa, M., et al. 2012, ApJ, 748, 142
Donley, J. L., Rieke, G. H., Pérez-González, P. G., Rigby, J. R., & Alonso-Herrero, A. 2007, ApJ, 660, 167
Dunne, L., Eales, S., Edmunds, M., et al. 2000, MNRAS, 315, 115
Dunne, L., Eales, S., Ivison, R., Morgan, H., & Edmunds, M. 2003, Nature, 424, 285
Dunne, L., & Eales, S. A. 2001, MNRAS, 327, 697
Hainline, L. J., Blain, A. W., Smail, I., et al. 2011, ApJ, 740, 96
Helou, G., Soifer, B. T., & Rowan-Robinson, M. 1985, ApJ, 298, L7
Howell, J. H., Armus, L., Mazzarella, J. M., et al. 2010, ApJ, 715, 572
Ishida, C. M. 2004, PhD thesis, Univ. Hawaii, (Source DAI-B 65/04)
Iwasawa, K., Sanders, D. B., Teng, S. H., et al. 2011, A&A, 529, A106
Jarrett, T. H., Chester, T., Cutri, R., Schneider, S. E., & Huchra, J. P. 2003, AJ, 125, 525
Kartaltepe, J. S., Sanders, D. B., Le Floc'h, E., et al. 2010, ApJ, 709, 572
Kennicutt, R. C., Jr., Armus, L., Bendo, G., et al. 2003, PASP, 115, 928
Komatsu, E., Dunkley, J., Nolta, M. R., et al. 2009, ApJS, 180, 330
Lacy, M., Storrie-Lombardi, L. J., Sajina, A., et al. 2004, ApJS, 154, 166
Landolt, A. U. 1983, AJ, 88, 439
Melbourne, J., Ammons, M., Wright, S. A., et al. 2008, AJ, 135, 1207
Perault, M. 1987, PhD thesis, Univ. Paris
Petric, A. O., Armus, L., Howell, J., et al. 2011, ApJ, 730, 28
Rodighiero, G., Daddi, E., Baronchelli, I., et al. 2011, ApJ, 739, L40
Salpeter, E. E. 1955, ApJ, 121, 161
Sanders, D. B., Mazzarella, J. M., Kim, D.-C., Surace, J. A., & Soifer, B. T. 2003, AJ, 126, 1607
Sanders, D. B., & Mirabel, I. F. 1996, ARA&A, 34, 749
Sanders, D. B., Soifer, B. T., Elias, J. H., et al. 1988, ApJ, 325, 74
Siebenmorgen, R., & Krügel, E. 2007, A&A, 461, 445
Skrutskie, M. F., Cutri, R. M., Stiening, R., et al. 2006, AJ, 131, 1163
Soifer, B. T., Sanders, D. B., Madore, B. F., et al. 1987, ApJ, 320, 238
Stern, D., Eisenhardt, P., Gorjian, V., et al. 2005, ApJ, 631, 163
Surace, J. A., & Sanders, D. B. 1999, ApJ, 512, 162
Surace, J. A., & Sanders, D. B. 2000, AJ, 120, 604
Surace, J. A., Sanders, D. B., & Evans, A. S. 2000, ApJ, 529, 170
Surace, J. A., Sanders, D. B., Vacca, W. D., Veilleux, S., & Mazzarella, J. M. 1998, ApJ, 492, 116
Takagi, T., Arimoto, N., & Hanami, H. 2003, MNRAS, 340, 813
Vavilkin, T. 2011, PhD thesis, Stony Brook Univ. (Proquest Dissertations and Theses No. AAT 347781)
Walcher, J., Groves, B., Budavári, T., & Dale, D. 2011, Ap&SS, 331, 1
Weingartner, J. C., & Draine, B. T. 2001, ApJ, 548, 296
Wuyts, S., Förster Schreiber, N. M., Lutz, D., et al. 2011, ApJ, 738, 106
Yuan, T.-T., Kewley, L. J., & Sanders, D. B. 2010, ApJ, 709, 884
Yun, M. S., Reddy, N. A., & Condon, J. J. 2001, ApJ, 554, 803